



A 2D Unified Distance Potential Field-Based Contact Interaction Algorithm for Combined Finite-Discrete Element Method (FDEM)

Weibing Cai¹ · Ke Gao^{1,2} · Shu-Gang Ai¹ · Yan Qiao³

Received: 15 April 2024 / Accepted: 7 January 2025

© The Author(s), under exclusive licence to Springer-Verlag GmbH Austria, part of Springer Nature 2025

Abstract

The combined finite-discrete element method (FDEM) has been widely used to simulate the rock fracturing process. However, the penalty-based contact interaction algorithm commonly utilized in FDEM is element size-dependent, which may yield artificial non-smoothness and abrupt jump of contact force. Specifically, the amplitude and direction of the obtained contact force between two contacting blocks can vary even when their overlap area is unchanged. To circumvent the limitations, we establish a unified distance potential field using the boundary node lists to calculate contact forces and consider the update of the local distance potential field when new fractures are generated. The proposed algorithm not only ensures momentum and energy conservation but also avoids the dependence of contact force on element size, which is thus suitable for any complex cases. The effectiveness and robustness of the proposed method for contact interaction between discrete bodies are verified, and its advantages are demonstrated. Finally, we present two application examples to demonstrate the capability of the proposed approach for evaluating rock slope stabilities when multi-block contact is involved. The work provides a new effective solution to analyze discontinuous computation models associated with complex rock mass systems.

Highlights

- We propose a 2D contact algorithm for FDEM based on a unified distance potential field.
- The unified distance potential field can be established using the boundary node lists.
- The distance potential field can also be updated when new fractures are generated.
- The proposed approach can avoid the dependence of contact force on element size.
- The accuracy of the proposed approach is verified and application examples are provided.

Keywords Combined finite-discrete element method (FDEM) · Contact force · Penalty function method · Unified distance potential field · Energy-conserving contact model

✉ Ke Gao
gaok@sustech.edu.cn

¹ Department of Earth and Space Sciences, Southern University of Science and Technology, Shenzhen 518055, Guangdong, China

² Guangdong Provincial Key Laboratory of Geophysical High-Resolution Imaging Technology, Southern University of Science and Technology, Shenzhen 518055, Guangdong, China

³ CNPC Engineering Technology R&D Company Limited, Beijing 102200, China

1 Introduction

Due to the presence of intermittent joints with different orientations and spacing, the rock masses are usually cut into arbitrary polygonal (convex or concave) blocks with various configurations (Zhou and Chen 2019). In the excavation processes of many rock engineering projects, such as rock slopes (Hatzor et al. 2004), underground mining (Regassa et al. 2018) and tunneling (Wu et al. 2018), the contact interaction between individual blocks with complex shapes has significant influences on the stability of rock mass systems. Therefore, accurate assessment and prediction of rock

block collisions are crucial for the safety of rock engineering construction.

As a powerful complement to analytical and experimental methods, numerical simulations, owing to their rapidity and convenience, have been extensively employed in recent years to describe the process of contact and collision of rock mass systems (Feng and Owen 2004; Gao and Feng 2019; Wang et al. 2021; Zheng et al. 2020a). Generally, according to the formulations of governing equations, contact approaches can be roughly classified into explicit and implicit categories (Zhao et al. 2018b). The most representative explicit approach is the discrete element method (DEM) proposed by Cundall and Strack (1979), which can explicitly simulate the complex contact interactions of discrete bodies even using simple constitutive models for the bonds compared with the finite element method (FEM). During the past thirty years, the commercial PFC (Particle Flow Code) software developed based on particle DEM has broad applications in brittle rock-related simulations owing to its simplicity of geometry and efficiency in contact detection. This method is not required to identify complex contact types. However, due to the lack of highly interlocked grain structures, the circular/spherical bodies utilized in PFC fail to simulate rocks with low strength ratios of tensile to uniaxial compressive strength (UCS) and high macro friction coefficients (Potyondy and Cundall 2004). To address this problem, a Flat-Joint Model was subsequently implemented in PFC to eliminate the particle rotation after breakage and enhance the interlock between adjacent particles, which has been successfully used in quantitative investigations of rock fracturing (Duan et al. 2021; Potyondy 2018). To accurately capture the particle shape, another commercial software UDEC based on the block DEM was developed, and the common plane (CP) method was proposed to deal with the various categories of contact scenarios, such as vertex-to-vertex, vertex-to-edge, and edge-to-edge contacts (Cundall 1988). However, this method yields an incomplete contact interaction algorithm due to the lack of a unified mechanical model for different contact cases (Zhao et al. 2018b). Particularly, for the vertex-to-vertex contact, the direction of normal contact force may encounter discontinuity and non-smoothness at the corner of polygon bodies, thereby causing local stress oscillation. Recently, as an alternative to UDEC, the Subspring Network contact model has been proposed to overcome the issues associated with circular particles, which also considers grain breakage and produces heterogeneity-induced local tension (Potyondy and Fu 2024).

The discontinuous deformation analysis (DDA), which adopts the implicit scheme to update the location and velocity of blocks, was first introduced by Shi and Goodman (1985) based on the minimum potential energy principle. In DDA, an open-close iteration scheme is used for contact detection, which repeatedly fixes and removes normal and

tangential springs between rock blocks (Zhao et al. 2018b). Consequently, the frequent variation of contact stiffness will significantly affect the stability of numerical modeling and reduce computational efficiency. Furthermore, similar to block DEM, DDA fails to guarantee a smooth transition of normal contact force direction under continuous movement of contact pairs. In addition, the implicit schemes require stable convergence of contact states, which may significantly increase the computation cost, especially for highly nonlinear dynamic impact problems (Zhao et al. 2018b; Zheng et al. 2020b).

In recent years, various improvements and efforts have been made to circumvent the deficiencies in the approaches mentioned above (Feng 2021a, b, c; Lai et al. 2022; Lei et al. 2020; Mathias et al. 2021; Nassauer and Kuna 2013; Zhao et al. 2018a). In these improvements, the magnitude and direction of contact force can be determined by the contact areas/volumes and the gradient of contact potential, respectively. These methods not only guarantee energy conservation in the process of elastic collision for arbitrarily shaped polygons/polyhedra but also can quickly determine the direction of normal contact force and the contact point (where the contact forces should be applied and according to which the total moment is zero). Among them, the combined finite-discrete element method (FDEM) (Munjiza 1992), which merges FEM-based analysis of continua with DEM-based contact processing for discontinua, provides an effective solution to handle complex contact or dynamic impact problems by meshing arbitrarily shaped polygons/polyhedra into an assembly of triangular/tetrahedral finite elements (Latham et al. 2019; Munjiza 2004).

In FDEM, the potential-based penalty function method was revolutionarily proposed to calculate the magnitude of normal contact force, and its direction can be directly determined by the gradient of contact potential (Munjiza 2004). Thus, the definition of contact potential plays a significant role in accurately measuring the penetrations between contact pairs. In the original form of FDEM, each 2D contactor triangular element is divided into three sub-triangles according to the location of the contact point, and the contact potential can be defined as the minimum shape functions at the contact point in the corresponding sub-triangle (Lei et al. 2020). Based on Green's formula, the calculation of the normal contact force of the contact area can be simplified into the integral of the potential on the boundary of the contactor element, and the direction of normal contact force can also be directly obtained based on the outward normal direction of element boundary (Munjiza 2004).

Nevertheless, two issues remain in the potential-based penalty function method. First, since the definition of potential is sensitive to element size, the amplitude of contact point potential is not always identical, even for scenarios with the same contact area, i.e., the generation of nonunique

contact force magnitudes. Second, although with the same direction of potential gradient, a jump in the direction of contact force may be encountered when the contact point moves from one sub-triangle to another. To solve these issues, a characteristic length of the mesh, instead of shape functions, is introduced to calculate the contact potential (Yan and Zheng 2017). This approach alleviates the dependence of contact force calculation on element size. Recently, based on the penetration distance between contact pairs, a distance potential function has been proposed to calculate the normal contact force (Zhao et al. 2018a, b). It is worth noting that the existing contact algorithms used in the FDEM can ensure the conservation of momentum and energy during the collision (Munjiza 2004; Yan and Zheng 2017; Zhao et al. 2018a, b). However, essentially, those methods work well when each discrete body is represented by a single finite element. If the boundary element (element on the boundary) contains inner nodes, i.e., a discrete body consisting of multiple inner finite elements, those methods fail to obtain accurate contact force due to the simple definition of contact point potential (as will be described in Sect. 2.1). Especially for relatively large contact areas between contact pairs, the normal contact force can even decrease with the increase of contact areas, which obviously contradicts the actual physics (as will be elucidated in Sect. 3.2.2). Additionally, a jump in contact force direction may be encountered when the contact point moves from one sub-triangle to another in the target element (as will be discussed in Sect. 3.2.3). Recently, an energy-conserving model has been developed in 2D FDEM to overcome the dependence of contact force on element size, which also resolves the non-smoothness of the contact force direction in some special situations (Cai et al. 2024). However, the approach may have problems estimating the nonlinear relationship between contact force and overlap areas. Moreover, it is difficult for this approach to determine the position of contact points for complex contact scenarios, especially for 3D modeling.

As an improvement, Lei et al. (2020) introduce a smooth potential field based on the finite element topology to solve the artificial non-smoothness and jump of contact force. Instead of using a “triangle-to-triangle” strategy, their method adopts “triangle-to-node” to calculate contact forces by discretizing the edges of target elements into Gaussian integration points (target points), making it suitable for both concave and convex bodies of complex shapes. However, the computational accuracy of this approach depends on the number of target points, and too many target points will reduce the computational efficiency. In addition, the appropriate number of target points for balancing computational accuracy and computational costs has not been fully elucidated. Importantly, the details of how to update local contact potential induced by crack initiation and propagation are not illustrated in their paper.

In this work, based on our in-house FDEM code, Pamuco, we establish a 2D unified distance potential field using the boundary node lists, in which the nodal contact potential of boundary elements is proportional to the shortest distance between each node and the solid boundaries. In the framework of the unified distance potential field, the calculation of contact force is systematically introduced. The rest of the paper is organized as follows. In Sect. 2, we first introduce the contact algorithm used in the conventional FDEM and elucidate its shortcomings. Then, we use the boundary node lists to establish a unified distance potential field for arbitrary-shaped polygons, and the update of the distance potential field associated with solid fracturing is also achieved. Following this, the calculations of normal and tangential contact force are introduced. In Sect. 3, we conduct a series of benchmark cases to verify the accuracy and robustness of the proposed method for contact interaction between discrete bodies, and the advantages of the proposed approach are also demonstrated. Subsequently, in Sect. 4, two typical cases are presented to demonstrate the capability of the proposed approach to evaluate the stability of rock mass systems. Conclusions are drawn in Sect. 5.

2 Unified Contact Distance Potential Field

In this section, contact algorithms used in the conventional FDEM are briefly introduced, and their drawbacks are demonstrated. Then, the proposed unified distance potential field is established by introducing the boundary node lists, and the update of the local distance potential field is realized when solid fracturing occurs. Finally, we introduce the formulation of normal and tangential contact force within the framework of the unified distance potential field.

2.1 Existing Contact Algorithms for FDEM

In 2D FDEM models for rocks, each discrete body is discretized into an assembly of triangular finite elements, and explicit time integration schemes are adopted to solve the nodal motion equations. The finite elements can deform, translate and rotate based on continuum mechanics principles and Newton’s second law. More details on the explicit time integration and the constitutive equations of finite elements are presented in Appendix A. The contact algorithm for processing the interaction between finite elements in contact in FDEM involves contact detection and contact interaction. The contact detection algorithm determines contact pairs (the two corresponding elements are denoted as contactor and target, respectively) using the efficient NBS (non-binary search) algorithm, which yields a theoretical CPU time proportional to the total number of finite elements (Munjiza and Andrews 1998). After obtaining

the contact pairs, the contact interaction algorithm will be performed to calculate the contact forces. The normal contact force is calculated based on the contact area of contact pairs, while the tangential contact force is determined by their relative slipping displacement. Both the normal and tangential contact forces are calculated in a penalty-based manner.

As sketched in Fig. 1, each of the two discrete bodies in touch is discretized into a series of triangular finite elements, then the contact between the two bodies can be simplified into contact between a series of triangular elements along the common boundaries. These boundary elements can be further grouped into contact pairs based on their relative positions, and two discrete bodies are denoted as target (E_{tar}) and contactor (E_{con}), respectively. The overlap area of E_{tar} and E_{con} is marked as S , and dA denotes the infinitesimal contact area. The normal contact force $d\mathbf{f}$ of dA is represented by (Munjiza 2004)

$$d\mathbf{f} = (\nabla\varphi_c(P_c) - \nabla\varphi_t(P_t))dA, \tag{1}$$

where P_c and P_t denote the point located in the target and contactor, respectively; the potential of points P_c and P_t are denoted by $\varphi_c(P_c)$ and $\varphi_t(P_t)$, respectively. The total normal contact force of the overlap area is calculated by (Munjiza 2004)

$$\mathbf{f}_c = \int_S (\nabla\varphi_c(P_c) - \nabla\varphi_t(P_t)) dA. \tag{2}$$

The target and contactor areas consist of m and n triangular finite elements, respectively. Then, $\varphi_c(P_c)$ and $\varphi_t(P_t)$ can be, respectively, obtained by summing the potentials of these finite elements involved (Munjiza 2004), i.e.,

$$\left. \begin{aligned} \varphi_c(P_c) &= \sum_{i=1}^m \varphi_c^i(P_c) \\ \varphi_t(P_t) &= \sum_{j=1}^n \varphi_t^j(P_t) \end{aligned} \right\} \tag{3}$$

The total normal contact force can be defined by (Munjiza 2004)

$$\mathbf{f}_c = \sum_{i=1}^m \sum_{j=1}^n \int_S (\nabla\varphi_c^i(P_c) - \nabla\varphi_t^j(P_t)) dA. \tag{4}$$

By replacing the integration over the area with the equivalent integration over the boundary, the total normal contact force can be further simplified into (Munjiza 2004)

$$\mathbf{f}_c = \sum_{i=1}^m \sum_{j=1}^n \int_{\Gamma} \mathbf{n}_{\Gamma} (\varphi_c^i(P_c) - \varphi_t^j(P_t)) d\Gamma, \tag{5}$$

where Γ represents the boundary of the overlap area of E_{tar} and E_{con} ; \mathbf{n}_{Γ} denotes the unit outward normal at the boundary.

For each triangular element, the point potential is defined as (Munjiza 2004)

$$\varphi_i(P) = \min \left\{ \frac{3A_1}{A}, \frac{3A_2}{A}, \frac{3A_3}{A} \right\}, \tag{6}$$

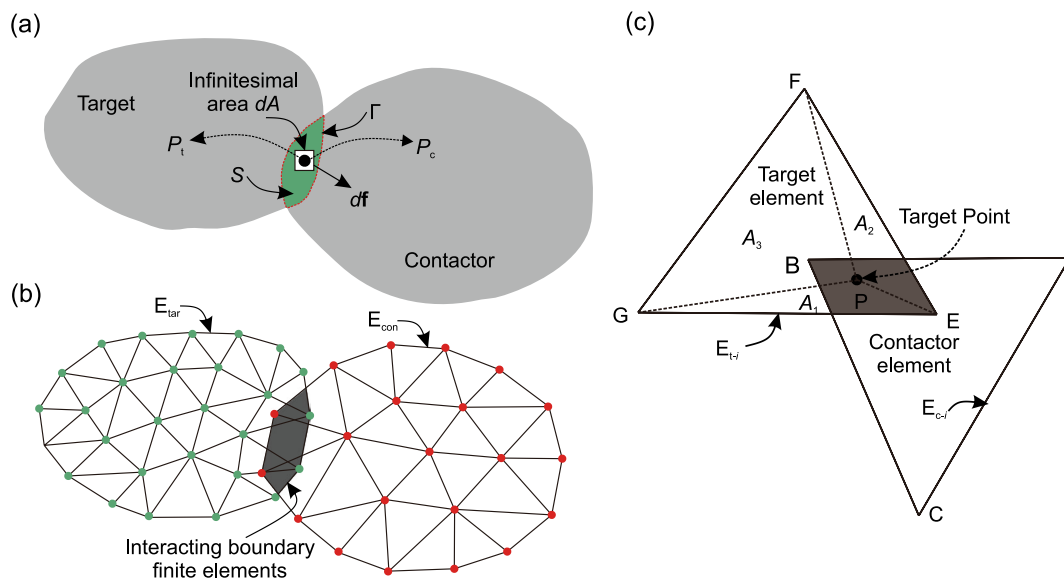


Fig. 1 **a** The repulsive force generated by a small penetration of two contacting solid domains. **b** Discretization of the two domains (i.e., E_{tar} and E_{con}). **c** Target (E_{t-i}) and contactor (E_{c-i}) elements

where A_1, A_2 and A_3 denote the areas of the sub-triangles constituted by point P and the three edges of the triangular element; A is the area of element E_{t-i} (see Fig. 1c). We notice that the calculation of point potential is crucial for accurately evaluating the normal contact force and should be proportional to the contact area between contact pairs. However, Eq. (6) fails to accurately calculate the point potential due to its dependence on element size. Taking the two scenarios presented in Fig. 2 for example, two triangular elements ΔABC and ΔHBC (share the same edge BC) penetrate the same element ΔDEF with the same contact area along the boundary of edge BC . Based on Eq. (6), the potential values of point D inside ΔABC and ΔHBC can be respectively given by

$$\begin{cases} \varphi(D_A) = \frac{S_{\Delta DBC}}{S_{\Delta ABC}} \\ \varphi(D_H) = \frac{S_{\Delta DBC}}{S_{\Delta HBC}} \end{cases}, \tag{7}$$

where $S_{\Delta DBC}, S_{\Delta ABC}$ and $S_{\Delta HBC}$ represent the areas of $\Delta DBC, \Delta ABC$ and ΔHBC , respectively. Here, assuming $S_{\Delta ABC} > S_{\Delta HBC}$, we have $\varphi(D_A) < \varphi(D_H)$, implying that the normal contact forces obtained in these two scenarios are different. However, this contradicts the fact that the normal contact forces in these two scenarios should be identical given the same contact area, indicating that the original

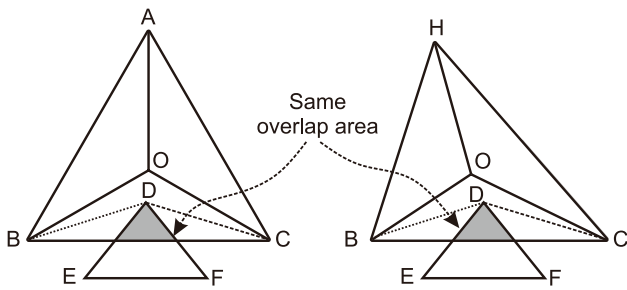


Fig. 2 Triangular element DEF penetrates the target elements ABC and HBC with the same contact area

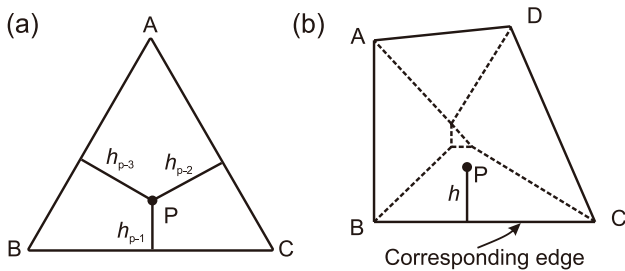


Fig. 3 Potential definition at point P using **a** Yan's approach (Yan and Zheng 2017) and **b** Zhao's approach (Zhao et al. 2018b). Sketches of the problems existing in these contact methods (i.e., Yan and Zheng 2017; Zhao et al. 2018b) in terms of **c** large penetration and **d** jump in

approach in FDEM has difficulty capturing accurate normal contact force. This original contact approach in FDEM is denoted as ‘‘Munjiza’s approach’’ hereafter.

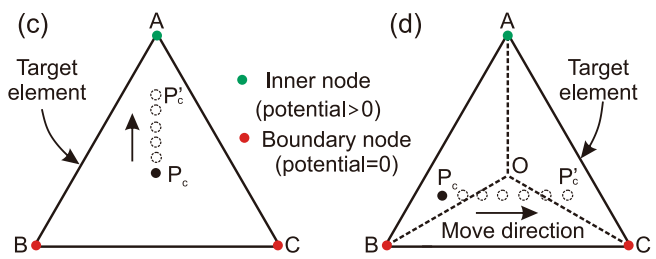
To address this problem, Yan and Zheng (2017) redefine the potential function in Eq. (6) so that the point potential is proportional to the shortest distance from a point to the three edges of a triangular element, i.e.,

$$\varphi_i(P) = \frac{1}{H} \min \{h_{p-1}, h_{p-2}, h_{p-3}\}, \tag{8}$$

where H is the standard embedded amount, which is generally taken as the minimum height of all the triangular elements; h_{p-1}, h_{p-2} and h_{p-3} are, respectively, the distance from point P to the three edges of the triangular element (see Fig. 3a). Similarly, Zhao et al. (2018b) define the distance potential at point P inside an arbitrary polygon as (Fig. 3b)

$$\varphi_i(P) = \begin{cases} 0, & P \text{ is outside the element} \\ \frac{h}{r}, & P \text{ is inside the element} \end{cases}, \tag{9}$$

where h is the distance between point P and the corresponding edge, and r denotes the radius of the maximum inscribed circle of the element. Although these two improvements can alleviate the influence of element sizes on contact force magnitude (Yan and Zheng 2017; Zhao et al. 2018a, b), two issues remain unsolved. First, the potential of contactor point P_c can decrease with the increase of penetration when the target element contains inner nodes (e.g., $\varphi(P_c) < \varphi(P'_c)$ in Fig. 3c), which may yield inaccurate contact force when the penetration between contact pairs is relatively large (e.g., exceeding half of the boundary element size). Second, a jump in contact force direction may be encountered when the contactor point moves from one sub-triangle to another in target element (e.g., contactor point P_c moves from sub-triangle ΔABO to ΔBCO in Fig. 3d). In fact, these two improved contact algorithms (Yan and Zheng 2017; Zhao et al. 2018a, b) (they altogether are denoted as Yan and Zhao’s approach hereafter) are more suitable for pure DEM applications, which may be inappropriate for FDEM



contact force direction. Contactor Point P_c is any point in the contactor element. Point P'_c denotes the movement trajectory of contactor point P_c via time

in which each discrete body can contain multiple inner finite elements (as will be illustrated in Sects. 3.2.2 & 3.2.3). Therefore, it is necessary to propose a new contact interaction method in the framework of FDEM to circumvent these existing deficiencies. Details of our proposed approach will be demonstrated next.

2.2 Nodal Distance Potential

In this section, we first establish two boundary node lists to calculate the nodal distance potential, which requires a theoretical CPU time proportional to the total number of boundary elements. Then, we show how to update the local nodal distance potential when solid fracturing occurs.

2.2.1 Establishment of Nodal Distance Potential

Theoretically, the nodal distance potential of a node is proportional to the shortest distance between the node and the solid domain boundary (Munjiza et al. 2011). The nodal distance potential for the boundary nodes is zero, while it is greater than zero for inner nodes associated with boundary elements (see Fig. 4). Note that the boundary nodes are the nodes on the boundary of the solid domain, while the

rest of the nodes are defined as the inner nodes. As long as an element contains a boundary node, it is considered as a boundary element, while the rest of the elements are defined as the inner elements. In other words, a boundary element may contain one or more boundary nodes, whereas the nodes of inner elements are all inside the solid domain.

Since the contact penalty used in FDEM is generally much larger (e.g., by $10\times$ or $100\times$) than the elastic modulus of model materials, the penetration between contact pairs is generally less than the size of boundary elements. To reduce the computational cost, we only calculate the nodal distance potential of nodes associated with boundary elements in the present study, i.e., only the boundary elements will participate in the contact detection and contact interaction (Fig. 4), which is similar to Munjiza’s and Yan and Zhao’s approach. This assumption is reasonable and could satisfy the majority of contact scenarios. Although rarely, we must admit that our proposed approach may yield inaccurate contact forces if the penetration is too large (e.g., exceeds the boundary element size). Moreover, if we obtain the nodal distance potential by looping over all boundary elements each time when new boundaries emerge (e.g., new fractures are generated), it no doubt requires demanding computational overhead. Here, we establish two boundary node lists to efficiently calculate the nodal distance potential.

We use the model presented in Fig. 5 as an example to elucidate the establishment of boundary node lists. Following the convention of FDEM, before the simulation, the solid domain shown in Fig. 5a is discretized into six triangular finite elements, and adjacent finite elements are connected with zero-thickness cohesive elements (Fig. 5b). We borrow the strategy introduced in our previous work using a master–slave manner (Cai et al. 2023) to obtain the mapping information from the original nodes before model discretization (denoted as master nodes, e.g., Node i_1 to i_6 in Fig. 5a) to the corresponding new nodes after model discretization (denoted as slave nodes, e.g., Nodes 0 to 11 in Fig. 5b). More details of the establishment of master–slave

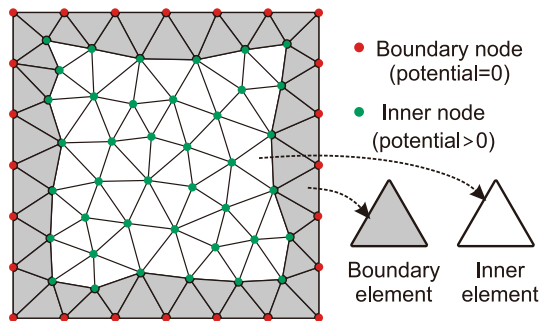


Fig. 4 A solid domain is discretized into a group of finite elements and nodes

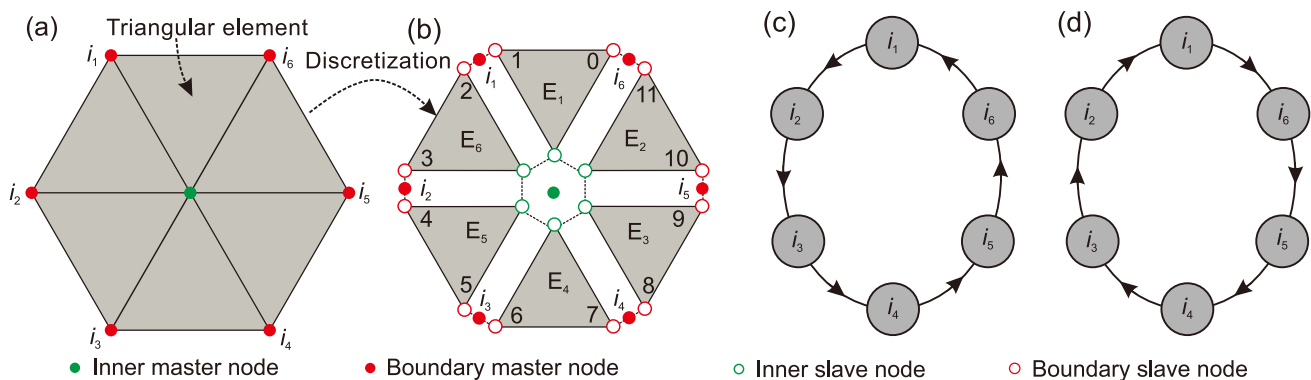


Fig. 5 a Solid domain. b Mesh discretization. Two master boundary node lists are established, i.e., c *BounNodeUP*[] and d *BounNodeDOWN*[]

node lists can refer to Appendix B. For example, the master Node i_1 corresponds to two slave Nodes 1 and 2. To establish the boundary node lists, we introduce two data structures for the boundary master nodes, which are named $BounNodeUP[]$ and $BounNodeDOWN[]$, respectively. For each boundary element containing only one inner node (e.g., the elements in Fig. 5b), we have $BounNodeUP[i_1]=i_2$ and $BounNodeDOWN[i_2]=i_1$. By looping over all boundary elements (e.g., E_1 to E_6 here), we can obtain two master boundary node lists (see Fig. 5c, d), i.e., $i_1 \rightarrow i_2 \rightarrow i_3 \rightarrow i_4 \rightarrow i_5 \rightarrow i_6 \rightarrow i_1$ and $i_1 \rightarrow i_6 \rightarrow i_5 \rightarrow i_4 \rightarrow i_3 \rightarrow i_2 \rightarrow i_1$. Note that the slave nodes corresponding to the same master node will displace together with their master node and share identical coordinates and nodal distance potential during the elastic deformation stage, i.e., the node binding scheme introduced in our previous work (Cai et al. 2023).

After establishing the boundary node lists, we can calculate the nodal distance potential of the inner nodes of boundary elements. Based on the number of slave boundary nodes in a boundary element, we can classify the boundary elements into three types, i.e., BoEle-1, BoEle-2 and BoEle-3, respectively denoting one, two and three boundary slave nodes contained in a single boundary element. For the boundary elements belonging to BoEle-1, e.g., $\Delta 012$ shown in Fig. 6a (node 1 is on the boundary), we only need to calculate the shortest distance from the inner slave node 0 or 2 to edges 45 and 78. First, we can find the master boundary node i_2 associated with the slave boundary node 1 based on the master–slave list; then, we continue to obtain the adjacent boundary master nodes i_1 and i_3 based on the boundary node lists, i.e., $BounNodeUP[i_2]=i_3$ and $BounNodeDOWN[i_2]=i_1$. If the shortest distance from the inner slave node 0 to edge i_1i_2 and i_2i_3 are denoted as d_{0-1} and d_{0-3} , respectively, we can obtain the nodal distance potential of slave node 0 using

$$\varphi(0) = \min \left\{ \frac{d_{0-1}}{r}, \frac{d_{0-3}}{r} \right\}, \tag{10}$$

where r is the maximal inscribed radius of all elements. Once the nodal distance potential of all inner slave nodes is obtained, we can further calculate the nodal distance potential of the inner master node (e.g., master node j_1) using

$$\varphi(j_1) = \min \{ \varphi(0), \varphi(3), \dots \}, \tag{11}$$

where $\varphi(0)$ and $\varphi(3)$ are the nodal distance potential of slave nodes 0 and 3, respectively. For the boundary elements belonging to BoEle-2, e.g., $\Delta 012$ shown in Fig. 6b, only the nodal distance potential of the inner slave node 0 needs to be calculated by finding the shortest distance from the slave node 0 to edges 12, 78 and 45. Similar to BoEle-1, the master boundary nodes i_1 and i_4 can be easily determined through the boundary node lists, e.g., $BounNodeUP[i_3]=i_4$

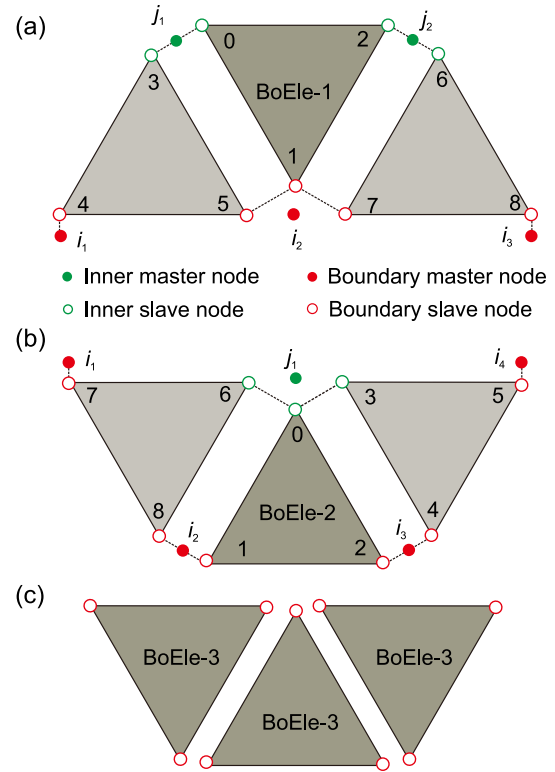


Fig. 6 Calculation of nodal distance potential when a boundary element contains **a** one (BoEle-1), **b** two (BoEle-2) and **c** three (BoEle-3) boundary nodes. A_1, A_2 and A_3 in **(a)** are the areas of the three sub-triangles constituted by point P_i and the three edges of the triangular element $\Delta 012$, respectively

and $BounNodeDOWN[i_2]=i_1$. Following this, the nodal distance potential of the inner master node j_1 can also be obtained.

Once the nodal distance potential of all inner nodes associated with boundary elements is obtained, we reach the final unified distance potential field. Continuing with the triangular finite element $\Delta 012$ shown in Fig. 6a as an example, for any point P_i inside $\Delta 012$, the corresponding potential can be calculated by

$$\varphi(P_i) = N_1\varphi(j_1) + N_2\varphi(i_2) + N_3\varphi(j_2), \tag{12}$$

where $\varphi(j_1)$, $\varphi(i_2)$ and $\varphi(j_2)$ are the nodal potential at master nodes j_1, i_2 and j_2 , respectively. N_1, N_2 and N_3 are the corresponding shape functions, i.e.,

$$N_1 = \frac{A_3}{A}; N_2 = \frac{A_1}{A}; N_3 = \frac{A_2}{A}, \tag{13}$$

where A_1, A_2 and A_3 denote the areas of the sub-triangles constituted by point P_i and the three edges of the triangular element; A is the total area of element $\Delta 012$ (see Fig. 6a). The established unified distance potential field of boundary elements for a convex and concave polygon solid domain

is shown in Fig. 7. It can be observed that the potential of the solid domain boundary is zero, while the largest nodal potential is distributed in the first layer of the inner nodes associated with boundary elements. The distance potential gradually increases when it is closer to the inner node of the boundary elements (Fig. 7b, d), demonstrating the reasonableness of the established unified distance potential field.

However, if all nodes of a triangular element are on the boundary (e.g., BoEle-3 in Fig. 6c), the distance potential of any point inside the triangular element cannot be directly calculated using Eq. (12). To address this problem, we insert a new inner node into the interior or boundary of a triangular

element to construct the unified distance potential field. For convenience, we choose the geometrical center point of the triangular element or the midpoint of the boundary as the inner node O (see Fig. 8a and c). Therefore, the potential of any point P_i inside the individual triangular element can be given by

$$\varphi(P_i) = N_{P_i} \varphi(O), \tag{14}$$

where $\varphi(O)$ is the nodal potential at node O that is determined by the shortest distance between node O and the solid boundary (e.g., edges AB, BC and CA in Fig. 8a), and N_{P_i} denotes shape function in terms of node P_i , which is obtained by the ratio of areas (e.g., $S_{P_i,BC}/S_{ABC}$ in Fig. 8a and $S_{P_i,DF}/S_{ODF}$ in Fig. 8c, where S denotes the areas of triangles). The distance potential field of a triangular element with all nodes on the boundary is presented in Fig. 8b, d.

2.2.2 Update of Nodal Distance Potential

When solid fracturing occurs, the finite elements on the two sides of broken cohesive elements will be marked as new boundary elements (see Fig. 9a). Therefore, it is necessary to update the local nodal distance potential to accommodate the contact interaction of these new fracture surfaces. Based on our previous work (Cai et al. 2023), we can easily obtain the new master nodes (i.e., i_6, i_7 and i_8 in Fig. 9a) based on the master–slave node mapping relationship. More details of the update of the master–slave list induced by solid fracturing are also presented in Appendix B. Taking the data structure of *BounNodeUP* for example, we have $BounNodeUP[i_4]=i_8, BounNodeUP[i_8]=i_7, BounNodeUP[i_7]=i_6$ and $BounNodeUP[i_6]=i_2$. Then, the boundary node list will be updated from $i_5 \rightarrow i_4 \rightarrow i_3 \rightarrow i_2 \rightarrow i_1$ to $i_5 \rightarrow i_4 \rightarrow i_8 \rightarrow i_7 \rightarrow i_6 \rightarrow i_2 \rightarrow i_1$. A similar procedure is performed to update the data structure of *BounNodeDOWN*. Finally, we only need to calculate the local nodal distance

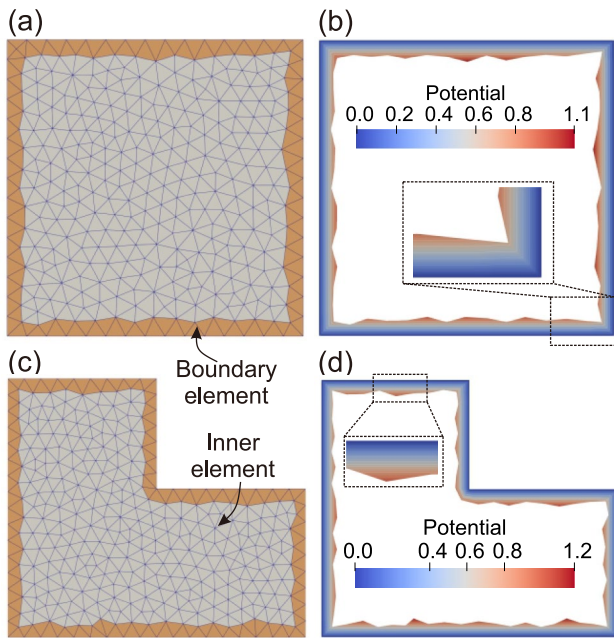


Fig. 7 Mesh and boundary and inner elements highlighted for **a** convex and **c** concave solid domain. Unified distance potential field of boundary element for **b** convex and **d** concave solid domain

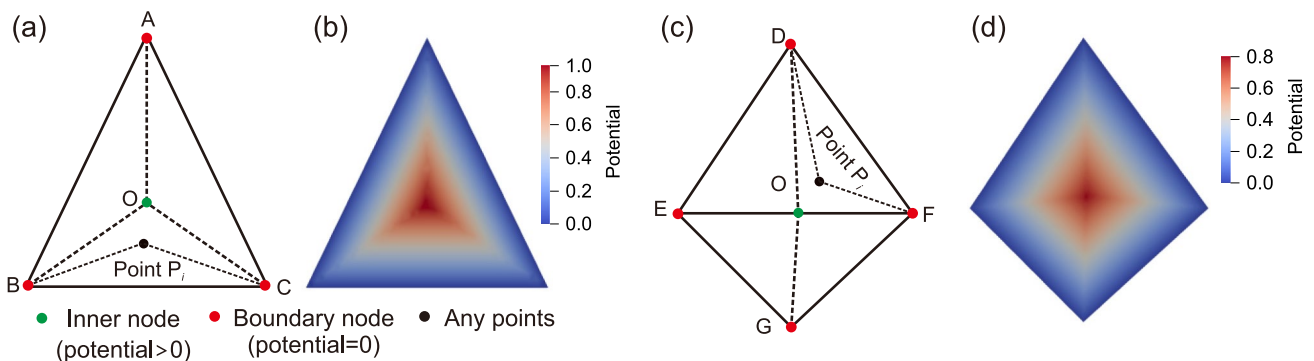


Fig. 8 Special cases for defining nodal distance potential field when all nodes of an element are on the boundary. **a** Inner node O is the geometrical center point of the triangular element. **c** Inner node O is

the midpoint of the boundary. The distributions of the nodal distance potential field for these two cases are presented in **(b, d)**, respectively. Point P_i denotes an arbitrary point inside the triangular element

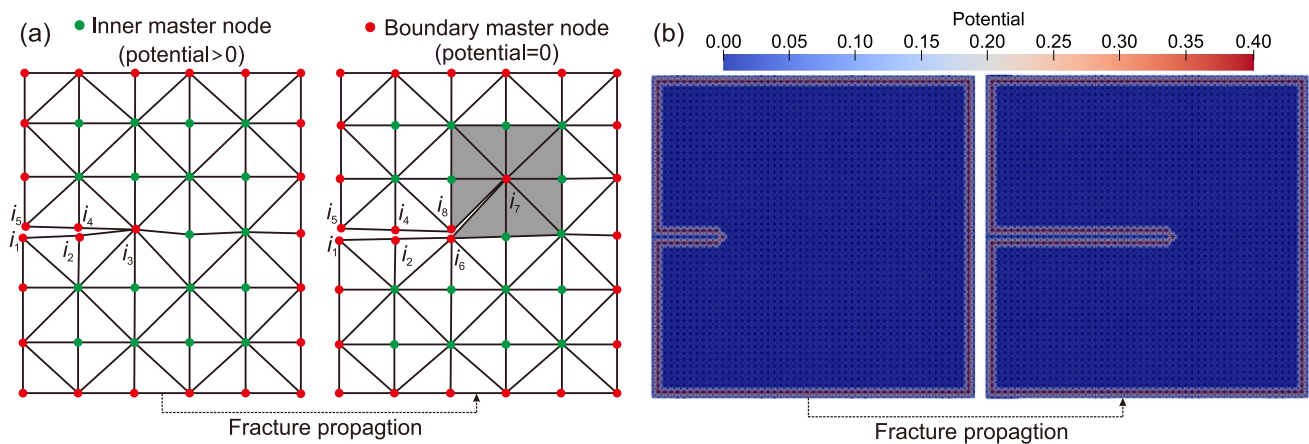


Fig. 9 **a** Boundary nodes updated under fracture propagation; the elements involved in nodal distance potential update are highlighted in gray. **b** An example of updating the distance potential field associated with fracture propagation

potential of these new boundary elements (see the gray patch in Fig. 9a) based on the updated boundary node lists. The implementation of the update of nodal distance potential is presented in Algorithm 1. An example of updating the

distance potential field of boundary elements associated with fracture propagation (towards the right direction) is sketched in Fig. 9b. Details on fracture initiation and propagation in FDEM can refer to Appendix C.

Algorithm 1 Update of nodal distance potential when solid fracturing occurs

-
- 1: **Update master-slave lists (see Appendix B)**
 - 2: **If** a cohesive element is broken **then**
 - 3: Generate new master nodes i_6, i_7, i_8 (see Fig. 9a)
 - 4: Find the corresponding slave nodes that belonged to new master nodes
 - 5: **end if**
 - 6: **Update boundary node list**
 - 7: **For** slave nodes of broken cohesive element **do**
 - 8: Update $BounNodeUP[]$:
 - 9: $BounNodeUP[i_4] = i_8, BounNodeUP[i_8] = i_7, BounNodeUP[i_7] = i_6, BounNodeUP[i_6] = i_2$
 - 10: Update $BounNodeDOWN[]$:
 - 11: $BounNodeDOWN[i_2] = i_6, BounNodeDOWN[i_6] = i_7, BounNodeDOWN[i_7] = i_8, BounNodeDOWN[i_8] = i_4$
 - 12: Mark new boundary elements and nodes
 - 13: **end for**
 - 14: **Update local nodal potential**
 - 15: **For** slave nodes of broken cohesive element **do**
 - 16: Find new boundary elements around the slave node
 - 17: **For** each node of finite element **do**
 - 18: Update local nodal potential using Eqs. (10) & (11)
 - 19: **end for**
 - 20: **end for**
-

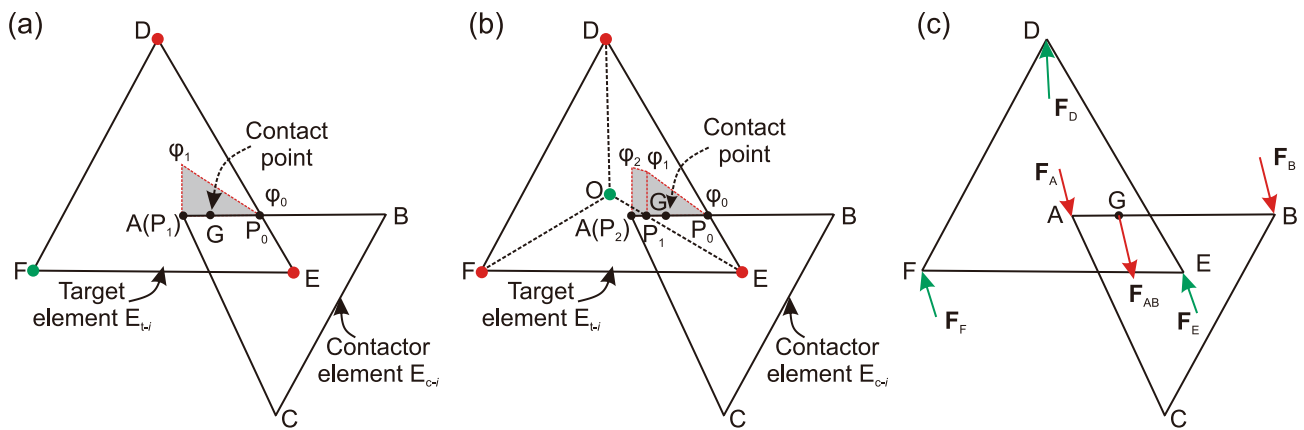


Fig. 10 Calculation of normal contact force. **a** The target element E_{t-i} contains inner nodes. **b** The nodes of the target element E_{t-i} are all on the boundary. **c** Equivalent nodal force. G represents the contact point (with respect to which the total moment is zero). The gray boxes denote the magnitude of normal contact force between target element E_{t-i} and edge AB

2.3 Formulation of Contact Force

After establishing the unified distance potential field, the normal contact force between contact pairs can be calculated. For the model shown in Fig. 10a, when the target element (E_{t-i}) contains one or two inner nodes, the normal contact force F_{AB} between target element E_{t-i} and edge AB can be directly calculated by

$$F_{AB} = \frac{1}{2} P_n \phi_1 L_1, \tag{15}$$

where P_n is the normal penalty parameter; ϕ_1 is the potential of point $P_1(A)$; L_1 is the distance between point P_1 and P_0 . Note that point P_0 is the intersection point of edge AB and target element E_{t-i} (see Fig. 10a), i.e., the potential of point P_0 is zero. The direction of F_{AB} is the outer normal of edge AB . The distance from contact point G (where the total moment is zero) to point A in Fig. 10a is $L_1/3$. Once the nodes of the target triangular element E_{t-i} are all on the boundary (see Fig. 10b), we also need to calculate the potential of intersections between edges AB and OE (i.e., point P_1 in Fig. 10b). Then, the normal contact force F_{AB} is modified as

$$F_{AB} = \frac{1}{2} P_n ((\phi_1 + \phi_2)L_1 + \phi_1 L_2), \tag{16}$$

where ϕ_1 and ϕ_2 are the potentials of points P_1 and $P_2(A)$, respectively; L_1 is the distance between points P_1 and P_2 ; L_2 is the distance between points P_1 and P_0 ; the direction of F_{AB} is the outer normal of edge AB . Note that the gray boxes in Fig. 10a, b are enclosed by the contact length (e.g., L_1 and L_2) and nodal potential (e.g., ϕ_1 and ϕ_2), which denotes the magnitude of normal contact force between target element E_{t-i} and edge AB . According to the moment balance with

respect to point A , the distance between contact point G and point A (Fig. 10b) is given by

$$L_{AG} = \frac{(4\phi_1 + 2\phi_2)L_1^2 + 3\phi_1 L_1 L_2 + \phi_1 L_2^2}{3[(\phi_1 + \phi_2)L_1 + \phi_1 L_2]}. \tag{17}$$

Again, points P_0 and P_1 are the intersection points of edge AB and the sub-triangle element. Then, with shape functions N_A, N_B, N_D, N_E and N_F , we can obtain the equivalent nodal force using (Munjiza et al. 2011)

$$\left. \begin{aligned} F_A &= N_A F_{AB} \\ F_B &= N_B F_{AB} \\ F_D &= N_D F_{AB} \\ F_E &= N_E F_{AB} \\ F_F &= N_F F_{AB} \end{aligned} \right\}. \tag{18}$$

As shown in Fig. 10c, the directions of F_A and F_B are consistent with F_{AB} , while the directions of F_D, F_E and F_F are opposite to F_{AB} . Here, $N_A + N_B = 1, N_D + N_F + N_E = 1$, which are associated with the position of contact point G . More details on the shape functions can be found in Munjiza's book (Munjiza et al. 2011).

The tangential contact force is calculated based on the relative slipping displacement between contact pairs and further updated using Coulomb's friction law. The relative velocity (V_{rG}) at contact point G (where contact force is applied and the total moment is zero) is given by Munjiza et al. (2011)

$$V_{rG} = V_{cG} - V_{tG}, \tag{19}$$

where V_{cG} and V_{tG} are the velocities of the contactor and target element at contact point G , respectively. These two can be, respectively, calculated by Munjiza et al. (2011)

$$\mathbf{V}_{cG} = N_A \mathbf{V}_A + N_B \mathbf{V}_B, \quad (20)$$

and

$$\mathbf{V}_{tG} = N_D \mathbf{V}_D + N_E \mathbf{V}_E + N_F \mathbf{V}_F \quad (21)$$

where \mathbf{V}_A , \mathbf{V}_B , \mathbf{V}_D , \mathbf{V}_E and \mathbf{V}_F are the node velocities shown in Fig. 11a. The tangential relative displacement increment (Δu_s) within one-time step (Δt) is given by Munjiza et al. (2011)

$$\Delta u_s = V_{rGt} \Delta t \quad (22)$$

where V_{rGt} is the projection of \mathbf{V}_{rG} on edge AB. The tangential contact force can be updated incrementally using (Munjiza et al. 2011)

$$\mathbf{F}_s = \mathbf{F}_s^{t-\Delta t} - P_s L_c \Delta u_s \quad (23)$$

where \mathbf{F}_s and $\mathbf{F}_s^{t-\Delta t}$ are tangential contact force at the current and previous time steps; P_s is the tangential penalty parameter; L_c is the contact length. As presented in Fig. 11b, if $|\mathbf{F}_s| \geq |\mathbf{F}_n| \mu$, the tangential contact force can be calculated based on Coulomb's friction law (Munjiza et al. 2011)

$$\mathbf{F}_s = \frac{\mathbf{F}_s}{|\mathbf{F}_s|} |\mathbf{F}_n| \mu \quad (24)$$

where \mathbf{F}_n is the normal contact force, and μ is the contact friction coefficient. At the same time, the current tangential slip (u_s) is updated by (Munjiza et al. 2011)

$$u_s = \frac{|\mathbf{F}_s|}{P_s L_c} \quad (25)$$

Similar to the normal contact force, the tangential contact forces can also be resolved to the nodes of the associated triangular elements. The same procedure of calculating the

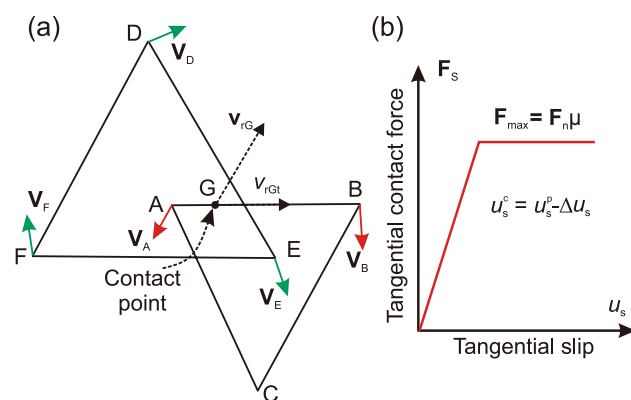


Fig. 11 Calculation of tangential contact force. u_s^c and u_s^p denote the tangential slip distance at the current and previous time step, respectively. \mathbf{F}_{\max} denotes the maximum tangential contact force

contact force between target element E_{t-i} and edge AB can be subsequently used to obtain the contact force acting on edges AC, ED and EF. Combining with the Cauchy stress of triangular elements in the previous time step, the nodal displacement and velocity in the current time step can be updated according to Eq. (A.4) to prepare for the next time step.

3 Verification and Comparison

In this section, several numerical experiments, such as those related to momentum conservation, energy conservation and frictional sliding, are first conducted to verify the accuracy of the proposed contact interaction algorithm. Then, we show the robustness of the proposed approach for the calculation of normal contact force in comparison to the existing contact algorithms in FDEM. The advantages of the proposed approach in terms of solid fracturing simulation and computational efficiency are also demonstrated through Brazilian tensile strength tests.

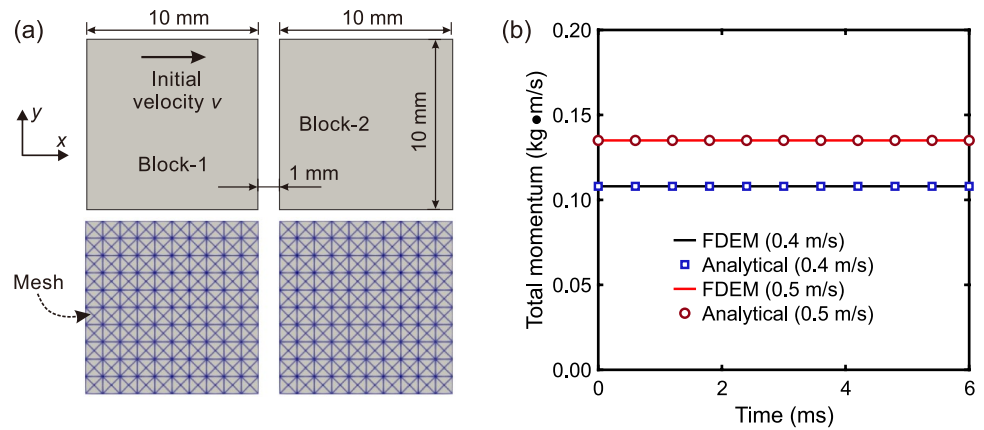
3.1 Verification

3.1.1 Momentum Conservation

Block collision tests are performed to verify the correctness of the proposed approach in terms of momentum conservation. As shown in Fig. 12a, the model consists of two identical square blocks (Block-1 and Block-2) with a length of 10 mm, and their surfaces are frictionless. The parameters used for the two blocks are as follows: Young's modulus $E = 30.0$ GPa, Poisson's ratio $\nu = 0.2$, bulk density $\rho = 2700$ kg/m³, viscous damping coefficient of finite element $\eta = 9.0 \times 10^3$ kg/m·s, contact penalty $P_n = P_s = 300$ GPa, and time step $\Delta t = 3.0 \times 10^{-8}$ s. Note that the viscous damping coefficient of finite elements is calculated using the equation $\eta = 2h\sqrt{E\rho}$ (E is Young's modulus, and ρ is bulk density) for all numerical cases (Tatone and Grasselli 2015). Each model consists of 1124 triangular elements with an average element size of 1 mm, and a structured triangulation mesh scheme is utilized. Gravity is ignored, and the total simulation time is 6×10^{-3} s.

For simplicity, we only consider the horizontal velocity (in the x direction) of each block, i.e., their vertical velocities (in the y direction) are fixed at zero. We set two initial x velocities ($v = 0.4$ m/s and 0.5 m/s) for Block-1 to hit against the initially static Block-2, and the initial horizontal gap between the two blocks is 1 mm. The mass center velocities of the two blocks are monitored for momentum calculation. The numerical results of the total momentum of Block-1 and Block-2 versus time for the two initial velocity scenarios are shown in Fig. 12b. It can be observed that

Fig. 12 **a** Initial configuration and mesh of the collision square blocks with identical geometry. **b** The total momentum of the two blocks in terms of analytical solution and FDEM simulation with two initial velocities for Block-1: $v=0.4$ m/s and $v=0.5$ m/s



the total momentum obtained from the FDEM simulation is consistent with the analytical solution. The maximum relative errors (i.e., the absolute difference between the FDEM simulated results and the analytical solution divided by the analytical solution) for the two scenarios are only 5.18×10^{-9} and 5.48×10^{-9} , respectively. Such minor relative errors verify the accuracy of our proposed approach in terms of momentum conservation.

3.1.2 Energy Conservation

We conduct collision tests to examine the accuracy of the proposed approach in terms of energy conservation. As presented in Fig. 13a, the model consists of a disk and a rectangle plate. The diameter of the disk is 20 mm, and the plate has dimensions of 40 mm \times 10 mm (width \times height). The plate is fixed, and we set different initial downward velocities ($v=0.45$ m/s, 0.50 m/s and 0.55 m/s) for the disk to collide with the plate. We use Young's modulus $E=30.0$ GPa, Poisson's ratio $\nu=0.25$, bulk density $\rho=2700$ kg/m³ and contact

penalty $P_n=P_s=300$ GPa in the model. Gravity and finite element viscous damping are not considered in this case. The model consists of 351 triangular elements with an average element size of 2.5 mm, and an unstructured Delaunay triangulation mesh scheme is utilized. The total simulation time of the numerical model is 3.5×10^{-4} s, with a time step of 6.0×10^{-8} s. The system's total kinetic energy E_k in the FDEM model can be calculated using

$$E_k = \sum_{i=1}^n \frac{1}{2} m_i v_i^2, \quad (26)$$

where m_i and v_i are respectively the nodal mass and nodal velocity for node i , and n is the total number of nodes in the system. The total kinetic energy versus time under different Block-1 initial velocities is shown in Fig. 13b. The kinetic energy of the system decreases first and then increases during the collision, which is consistent with previous observations (Fukuda et al. 2019; Lei et al. 2020). For the three Block-1 initial velocities, the maximum relative errors (i.e.,

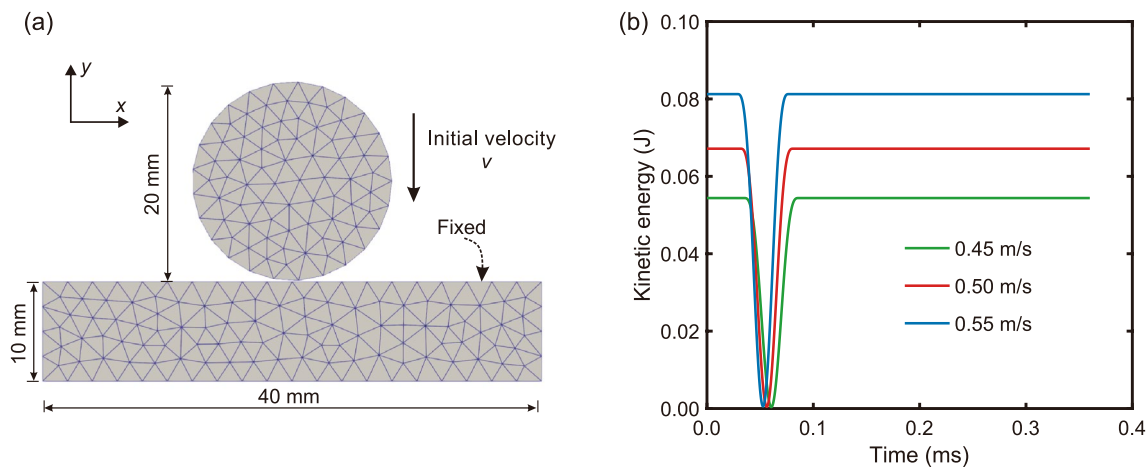


Fig. 13 **a** Model geometry and loading conditions. **b** The system's total kinetic energy with time under different initial velocities (v) for Block-1

the absolute kinetic energy differences from pre to post-impact divided by the initial kinetic energy for the impacting sphere) are only 8.36×10^{-6} , 1.14×10^{-5} and 1.34×10^{-5} , respectively, confirming that the proposed approach is energy-conserving for elastic collision.

3.1.3 Frictional Experiment

The classic test of a sliding block on an inclined plane is used to verify the accuracy of the proposed approach in terms of block sliding (Fig. 14a). The model consists of a small square block (Block-1) and a large rectangle block (Block-2) at the bottom. The length of Block-1 is 10 mm, and Block-2 has dimensions of 90 mm \times 10 mm (width \times height). Block-1 slides along the upper surface of Block-2 under gravity, and Block-2 is fixed. The parameters used for the model are as follows: Young's modulus $E = 30.0$ GPa, Poisson's ratio $\nu = 0.25$, bulk density $\rho = 2333$ kg/m³, finite element viscous damping coefficient $\eta = 2.4 \times 10^4$ kg/m \cdot s, contact penalty $P_n = P_s = 300$ GPa, and time step $\Delta t = 6.0 \times 10^{-8}$ s. The model consists of 1,260 triangular elements with an average element size of 2.5 mm, and an unstructured Delaunay triangulation mesh scheme is utilized (Fig. 14b). The total simulation time of the model is 1.44 s.

If the friction angle between the two blocks is smaller than the inclination angle of Block-2, the analytical solutions for the spatial evolution of displacement s and velocity v of Block-1 along the upper surface of Block-2 are respectively given by

$$s = \frac{1}{2}g(\sin \psi - \mu \cos \psi)t^2, \quad (27)$$

and

$$v = g(\sin \psi - \mu \cos \psi)t, \quad (28)$$

where g is the gravitational acceleration, μ denotes the friction coefficient between Block-1 and Block-2, and ψ is the inclined angle of Block-2 with respect to the horizontal line (anticlockwise positive from right). Here, $g = -9.8$ m/s², $\psi = 30^\circ$. The evolutions of the displacement and velocity of Block-1 along the upper surface of Block-2 for three friction coefficients between the two blocks ($\mu = 0.0, 0.2$ and 0.4) are shown in Fig. 15. It can be observed that the maximum relative errors for displacement and velocity are only 3.32×10^{-8} and 3.45×10^{-8} , respectively, verifying the accuracy of the proposed approach for block sliding contact simulation.

3.2 Comparison

3.2.1 Mesh Size Dependency

As mentioned in previous works (Yan and Zheng 2017; Zhao et al. 2018a, b), the potential definition of Munjiza's approach is sensitive to element size (see Sect. 2.1). Here, we perform a series of collision tests to compare the normal contact force obtained from Munjiza's approach, Yan and Zhao's approach and our proposed approach under the same contact area. As shown in Fig. 16a, the model contains one small square block (Block-1) at the top and a large rectangle block (Block-2) at the bottom. The length of Block-1 is 10 mm, and Block-2 has dimensions of 90 mm \times 10 mm (width \times height). During the simulation, Block-2 is fixed, and Block-1 collides with Block-2 with a constant downward velocity of 0.05 m/s (i.e., -y direction). We set five loading points with a distance of 15 mm for Block-1, i.e., points A, B, C, D and E shown in Fig. 16a, to test the simulated normal contact force. The contact areas between Block-1 and Block-2 at each specific time are the same for the five loading point scenarios.

The parameters used for the model are as follows: Young's modulus $E = 30.0$ GPa, Poisson's ratio $\nu = 0.27$, bulk density

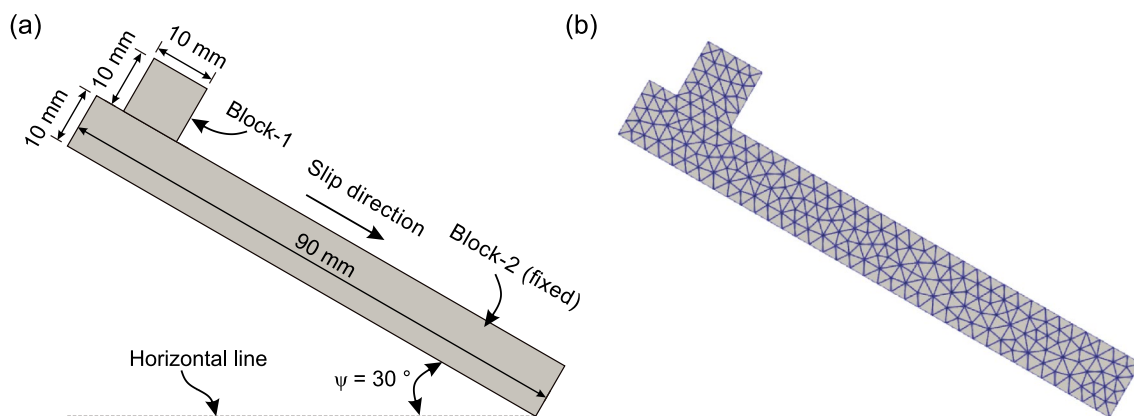


Fig. 14 a Initial configuration of the numerical frictional experiment. b Mesh

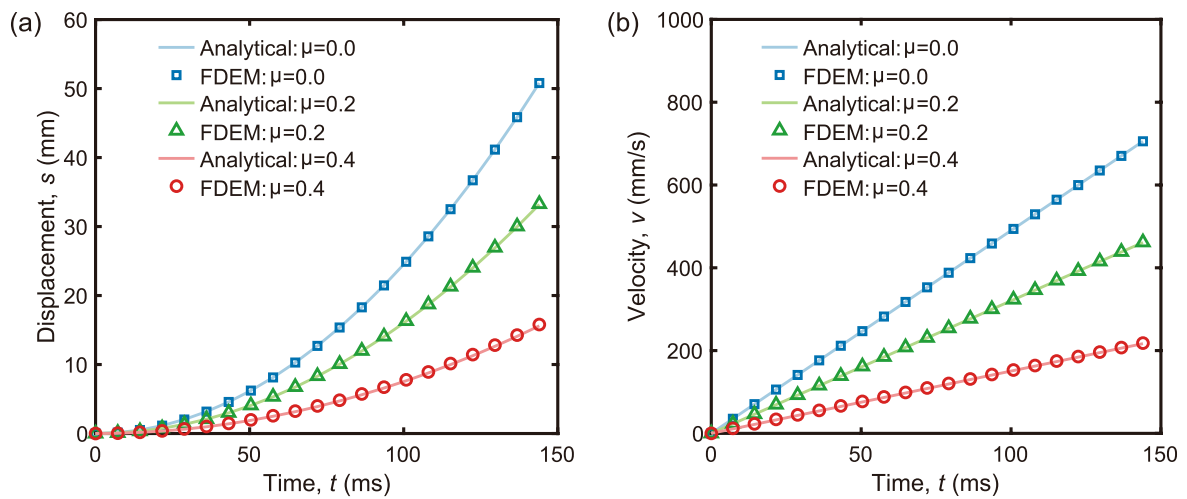


Fig. 15 **a** Displacement and **b** velocity of Block-1 along the top surface of Block-2 for different friction coefficients between the two blocks ($\mu=0.0, 0.2$ and 0.4)

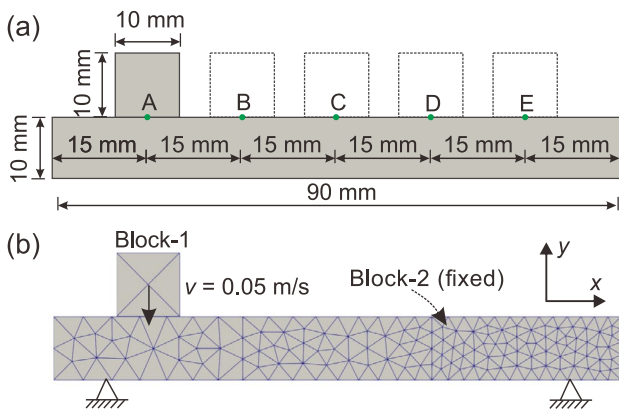


Fig. 16 **a** Model geometry and the five contact scenarios. **b** Mesh

$\rho = 2700 \text{ kg/m}^3$, contact penalty $P_n = P_s = 300 \text{ GPa}$, finite element viscous damping coefficient $\eta = 9.0 \times 10^4 \text{ kg/m}\cdot\text{s}$, and time step $\Delta t = 6.0 \times 10^{-8} \text{ s}$. Gravity is not considered, and the model consists of 279 triangular elements with an average size of 3.34 mm. Unstructured Delaunay triangulation mesh scheme is utilized, and the element size of Block-2 gradually decreases from left to right (see Fig. 16b).

As presented in Fig. 17a, for Munjiza’s approach, although the contact area for scenarios at each loading point is identical at each specific time, the normal contact forces for the five scenarios are different, manifesting the dependence of Munjiza’s approach on element size. For Yan and Zhao’s approach, the normal contact force remains unchanged with a small penetration. However, the dependence of contact force on mesh size is also encountered when the penetration is relatively large (see Fig. 17b). For our proposed approach, the obtained normal contact forces are the

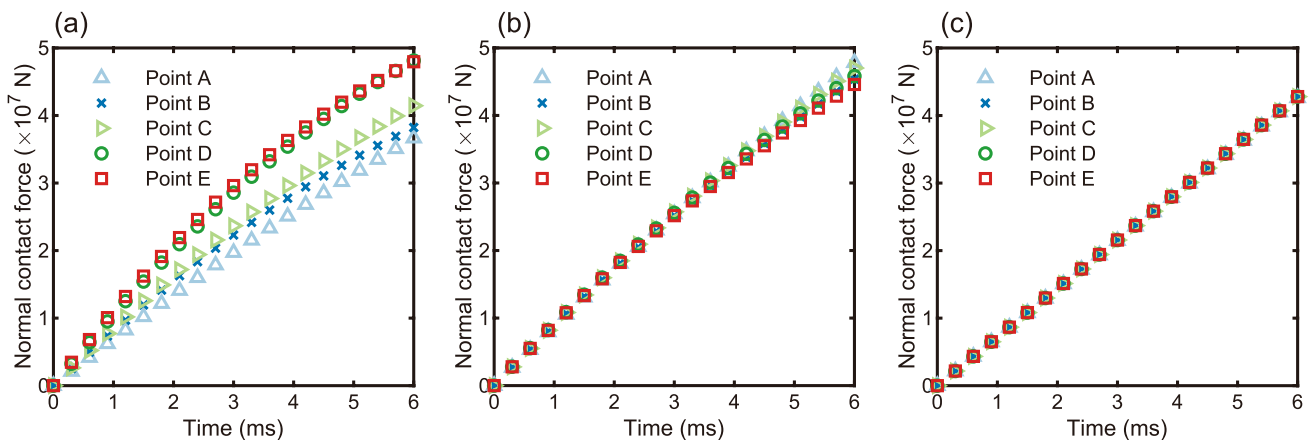


Fig. 17 Comparison of the simulated normal contact forces using **a** Munjiza’s approach, **b** Yan and Zhao’s approach, and **c** our proposed approach

same for the five scenarios, and they also linearly increase with the increase of contact area (Fig. 17c), verifying the independence of the proposed approach on element size for normal contact force calculation.

3.2.2 Large Contact Area Test

As mentioned in the Introduction section and Fig. 3c, some recently improved contact algorithms for FDEM (Yan and Zheng 2017; Zhao et al. 2018a, b) also fail to obtain accurate contact force when the penetration of the boundary element is relatively large (e.g., exceeding half of the boundary element size). To compare the normal contact force calculated by Yan and Zhao's approach and our proposed approach for a relatively large contact area (but less than the boundary element size) between contact pairs, a contact test containing one small square block (Block-1) and a large rectangle block (Block-2) is performed (see Fig. 18a). The dimensions of Block-1 and Block-2 are 10 mm × 15 mm and 30 mm × 20 mm, respectively. Block-1, with a constant downward velocity of 0.3 m/s (i.e., -y direction), is designated to collide with the fixed Block-2, and the selection of this velocity creates an extreme contact situation, i.e., a relatively large contact area between the two blocks. The parameters used for the model are as follows: Young's

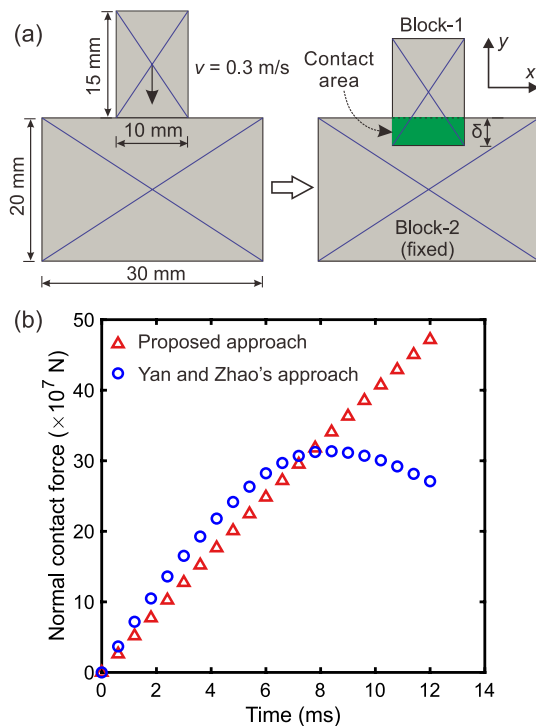


Fig. 18 **a** Initial geometric configuration of the model. **b** Normal contact force with time for both the proposed approach and Yan and Zhao's approach. δ denotes the penetration distance (along -y direction) between the two blocks

modulus $E = 30.0$ GPa, Poisson's ratio $\nu = 0.25$, bulk density $\rho = 2700$ kg/m³, contact penalty $P_n = P_s = 300$ GPa, finite element viscous damping coefficient $\eta = 9.0 \times 10^4$ kg/m·s, and time step $\Delta t = 2.0 \times 10^{-7}$ s. Gravity is not considered in this case. Each block consists of four triangular elements, and the total simulation time is $t = 0.012$ s. The penetration between the two blocks reaches $\delta = vt = 3.6$ mm at the end.

As shown in Fig. 18b, with the increasing contact area, the normal contact force calculated using Yan and Zhao's approach increases nearly linearly at the beginning and decreases slightly close to the end. This contradicts the physics that the normal contact force should theoretically increase with the increasing contact area. In our proposed unified distance potential field, we can observe a linear increase of normal contact force with the increasing contact area, verifying the applicability and robustness of the proposed approach for simulations with relatively large contact areas. It should be emphasized again that our proposed approach may yield inaccurate contact forces when the penetration exceeds the boundary element size due to the nodal distance potential of nodes of inner elements not being calculated.

3.2.3 Normal Contact Force Direction

As previously pointed out in Fig. 3d, a jump in contact force direction may occur when the contact point moves from one sub-triangle to another using Yan and Zhao's approach. Here, we use two overlapped equilateral triangle finite elements (Block-1 and Block-2), with a side length of 10 mm and 5 mm, respectively, to test the correctness of the proposed approach for contact force direction calculation. As shown in Fig. 19a, Block-2 with a constant velocity of 0.05 m/s is designed to impact the fixed Block-1 along the x axis direction, which forms a constant overlap area between the two blocks during the sliding process. The parameters used are as follows: Young's modulus $E = 30.0$ GPa, Poisson's ratio $\nu = 0.25$, bulk density $\rho = 2700$ kg/m³, contact penalty $P_n = P_s = 300$ GPa, and finite element viscous damping coefficient $\eta = 7.8 \times 10^4$ kg/m·s. The total simulation time is 0.117 s with time step $\Delta t = 2.6 \times 10^{-7}$ s. Note that the gravity and contact friction between the two blocks are not considered.

For convenience, the intersection angle between the calculated normal contact force direction and the x axis is denoted as γ (anticlockwise positive from the right). The evolution of the normal contact force direction with time using the proposed approach and Yan and Zhao's approach is shown in Fig. 19b. For Yan and Zhao's approach, we can observe that γ gradually increases when the location of contact transits from sub-triangles ΔDEO to ΔEFO , and then γ gradually decreases when transiting from ΔEFO to ΔFDO . This demonstrates that the calculated normal contact force

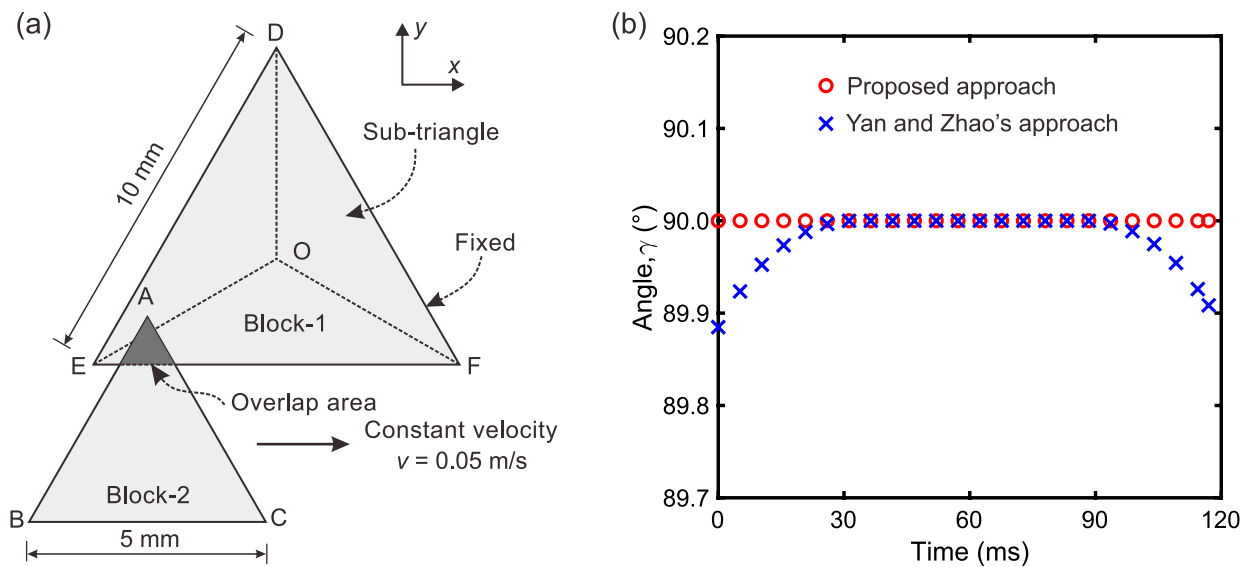


Fig. 19 **a** Model geometry. **b** Evolution of the normal contact force direction with time for the proposed approach and Yan and Zhao's approach. γ denotes the intersection angle between the calculated normal contact force direction and the x axis

direction using Yan and Zhao's approach deviates from the y direction (i.e., $\gamma=90^\circ$) when Block-2 is located near the two sides (i.e., edges OE and OF) of sub-triangle $\triangle EFO$. However, the simulated normal contact force direction obtained by the proposed contact algorithm remains unchanged at $\gamma=90^\circ$ during the sliding process. This is consistent with the physics that the geometric features between the two blocks should be constant. Therefore, the proposed contact algorithm can effectively overcome the incorrect jump in the direction of normal contact force.

3.2.4 Brazilian Tensile Test

We perform Brazilian tensile tests to compare the Munjiza's and the proposed approach, with the purpose of evaluating our proposed approach for contact interaction processing along with fracture propagation. The model consists of two loading plates and a rock specimen, and the diameter of the rock specimen is 50 mm (see Fig. 20a). The axial loads are imposed on the specimen by moving the two plates inwards at a constant velocity of 0.05 m/s. This selected velocity can ensure the quasi-static loading of Brazilian tensile tests (Mahabadi et al. 2012; Tatone and Grasselli 2015). The model consists of 14,528 triangular

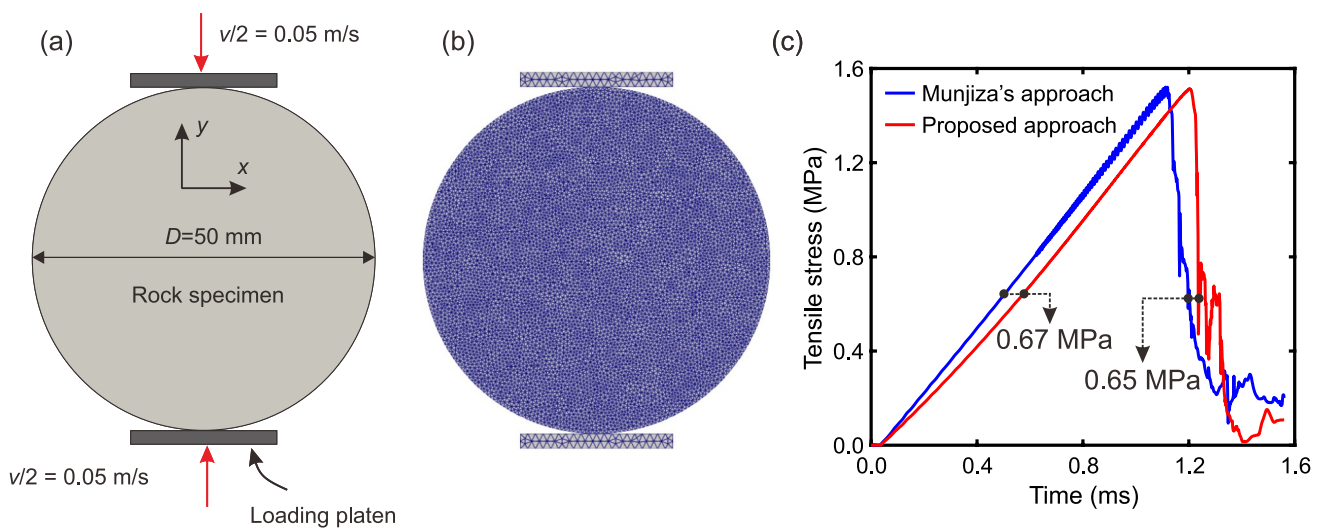


Fig. 20 **a** Model geometry and boundary conditions. **b** Mesh. **c** Comparison of tensile stress for Munjiza's approach and the proposed approach

Table 1 Input parameters for the Brazilian tensile test (Liu and Deng 2019)

| Input parameters | Values |
|---|--------|
| Young's modulus, E (GPa) | 12.5 |
| Bulk density, ρ (kg/m ³) | 2400 |
| Poisson's ratio, ν | 0.25 |
| Viscous damping coefficient, η (kg/m·s) | 2800 |
| Tensile strength, f_t (MPa) | 1.5 |
| Cohesion, c (MPa) | 8 |
| Internal friction angle, φ (°) | 30 |
| Mode I fracture energy, G_{f1} (J/m ²) | 8 |
| Mode II fracture energy, G_{f2} (J/m ²) | 60 |
| Normal contact penalty, P_n (GPa) | 18 |
| Tangential contact penalty, P_s (GPa) | 18 |
| Cohesive penalty, P_f (GPa) | 62.5 |
| Sample-plate friction coefficient, k_1 (-) | 0.1 |
| Sample friction coefficient, k_2 (-) | 0.7 |

elements with an average element size of 0.76 mm, and the unstructured Delaunay triangulation mesh scheme is utilized (Fig. 20b). The rock specimen is assumed to be homogeneous and isotropic, and the time step is 1.2×10^{-8} s. The input parameters for the FDEM simulations are tabulated in Table 1 and calibrated in previous work (Liu and Deng 2019).

The comparison of evolving tensile stresses for Munjiza's and the proposed approach is presented in Fig. 20c. The tensile stress, σ_t , of the rock specimen is calculated using (Liu and Deng 2019)

$$\sigma_t = \frac{2F_c}{\pi Dm}, \quad (29)$$

where F_c is the contact force between the loading plates and rock specimen; D and m are respectively the diameter and thickness (set as one unit here) of the rock specimen. As shown in Fig. 20c, tensile stress oscillations prior to peak stress are observed in Munjiza's approach, which may be caused by the inaccurate evaluation of contact force (F_c) between the loading plates and the rock specimen since the tensile stress is determined by the contact force (see Eq. (29)) (Yan and Zheng 2017). For our proposed approach, the tensile stress increases smoothly with the increase of diametric displacement before peak stress, verifying the robustness of the proposed approach for contact force calculation. Compared to Munjiza's approach (1.522 MPa), the peak tensile strength obtained using our proposed approach (1.512 MPa) is relatively closer to the prescribed tensile strength of the rock specimen in the numerical models (1.5 MPa in Table 1).

To further compare the difference between Munjiza's and the proposed approach, we select two typical stress levels where the tensile stresses reach 0.67 MPa and 0.65 MPa, respectively, representing the stress states before and after the peak strength (see Fig. 20c). When the tensile stress drops to 0.65 MPa (after the peak tensile stress), the crack number obtained using the proposed approach is slightly less than that of Munjiza's approach; however, the crack propagation paths from the two approaches are similar except for locations near the loading plates (Fig. 21a, b), indicating that the failure pattern difference of Brazilian tensile tests obtained by the two approaches is insignificant. The distance potential fields in our proposed approach at the two selected tensile stress levels (0.67 MPa and 0.65 MPa) are presented

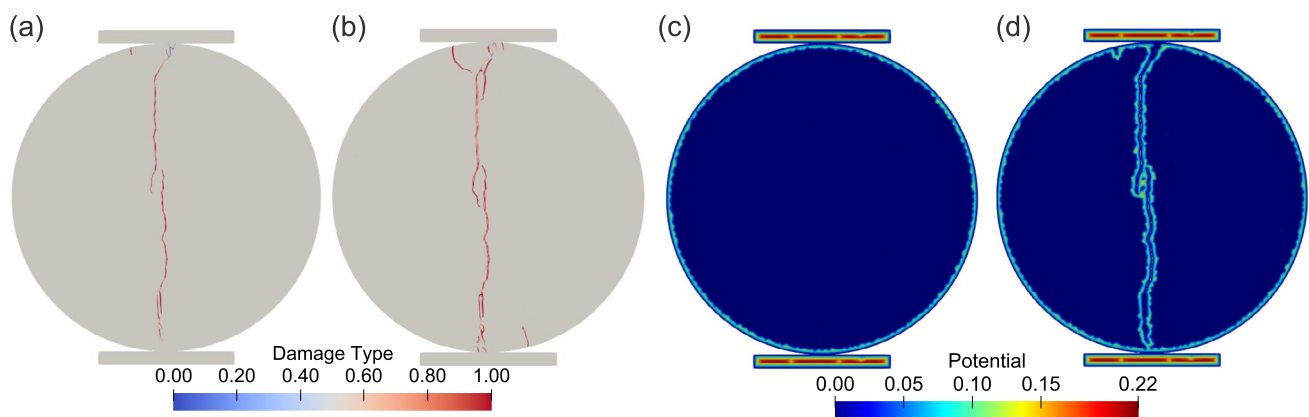


Fig. 21 Crack patterns for **a** the proposed and **b** Munjiza's approach when tensile stress drops to 0.65 MPa (after the peak tensile stress). The distance potential field of the model at different loading points: **c** 0.67 MPa (before peak tensile stress) and **d** 0.65 MPa (after peak tensile stress) in the proposed approach. The 'Damage Type' varies

from 0 to 1, where '0' and '1' respectively denote the pure shear and pure tensile cracks associated with the broken cohesive elements. More details on crack initiation and propagation in FDEM are available in Appendix C and Munjiza's books (Munjiza 2004; Munjiza et al. 2011)

in Fig. 21c, d, from which we can observe the change of the local distance potential field together with the crack propagation, which confirms the robustness of the proposed approach for the distance potential field updating.

We continue to use the specimen shown in Fig. 20a as an example to compare the computational efficiency between Munjiza's approach and our proposed approach. A variable r_{effi} is proposed to denote the ratio of computing time needed between Munjiza's and the proposed approach upon the tensile stress dropping to 90% of the peak stress. The diameter of the specimen and average element size are denoted as D and h , respectively, and an increasing D/h represents

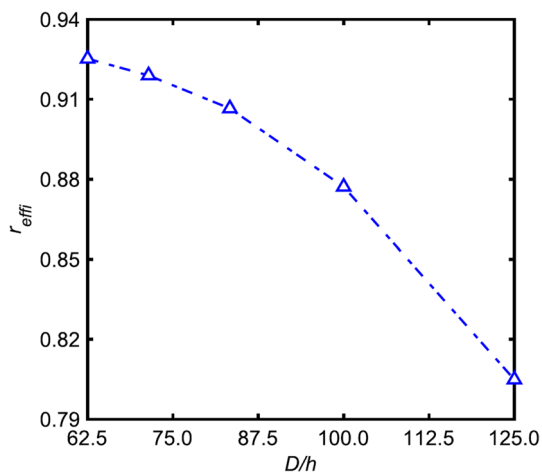


Fig. 22 Comparison of computational efficiency between the proposed and Munjiza's approach with various element sizes. D denotes the diameter of the Brazilian disc and h is the average element size

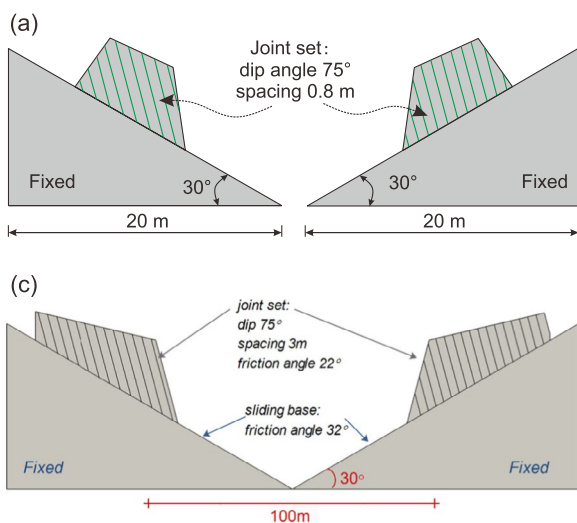


Fig. 23 **a** The model of rock slopes in a valley cut by a set of through joints. **b** The velocity distribution of the rock slope model after 2.2 s. **c** The model of rock slopes in a valley cut by a set of persistent joints

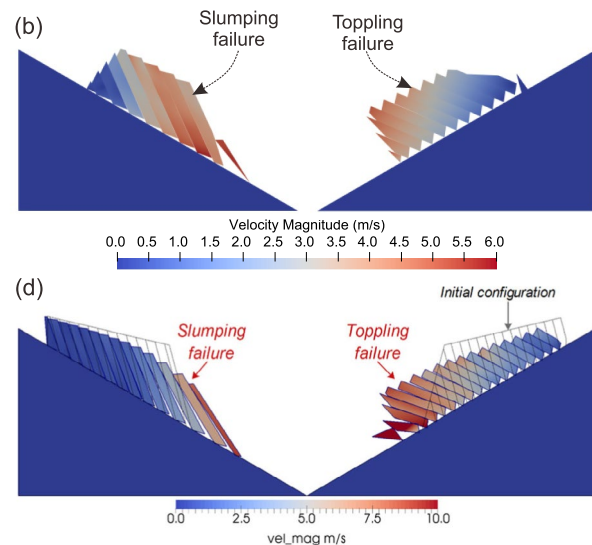
an increase in the number of finite elements in the model. As shown in Fig. 22, with the increase of D/h , r_{effi} gradually decreases and reaches around 0.8 for $D/h = 125$ (about 32,229 triangle elements). Therefore, the proposed approach is slightly more computationally expensive than Munjiza's approach, and such computational cost increase for our proposed approach is more significant with the increasing number of finite elements due to the frequent update of boundary node lists when solid fracturing occurs.

4 Application Examples

In this section, two typical cases are employed to demonstrate the capability of the proposed approach in evaluating the failure process of rock masses involving contact. Since we only focus on the contact interaction between rock blocks, no rock fracturing is considered here.

4.1 Rock Toppling and Slumping

In this section, rock slopes in a valley region are established to evaluate the capability of the proposed approach in simulating the slope failure patterns. As shown in Fig. 23, the valley consists of rock slopes with triangular sliding bases, in which the rock slopes are cut by a joint set with a dip angle of 75° and spacing of 0.5 m. The bottom lengths of the two sliding bases with an inclined angle of 30° are 20 m. The parameters used for this model are as follows: Young's modulus $E = 30.0$ GPa, Poisson's ratio $\nu = 0.27$, bulk density $\rho = 2700$ kg/m³, gravitational acceleration $g = -9.8$ m/



and **d** simulated results of rock slope after 3.5 s from the previous simulation (Zheng et al. 2020b)

s^2 , contact penalty $P_n = P_s = 300$ GPa, finite element viscous damping coefficient $\eta = 6.0 \times 10^5$ kg/m·s, and time step $\Delta t = 2.0 \times 10^{-6}$ s. The model consists of 16,780 triangular elements with an average element size of 0.35 m, and the total simulation time is 2.2 s. The friction angle between the rock slope and the sliding base is set as 32° , indicating that the rock slope will not slide along the base. However, the rock slope will fail due to the existence of a joint set with a friction angle of 22° between joint surfaces (Zheng et al. 2020b). As shown in Fig. 23b, the left rock slope falls in a slumping pattern, while the right part features a toppling pattern. These failure processes are consistent with previous studies (Zheng et al. 2018; Zheng et al. 2020a, b) (see Fig. 23c, d), verifying the proposed approach's feasibility in simulating complex rock block behaviors.

4.2 Vaiont Landslide

The Vaiont landslide (Sitar et al. 1997) that occurred in northern Italy is employed to further simulate the rock

slope sliding process at the engineering scale. The profile of the Vaiont landslide before and after the slide is presented in Fig. 24a, where the rocks slip along the sliding surface under gravity. The parameters used are as follows: Young's modulus $E = 10$ GPa, Poisson's ratio $\nu = 0.3$, bulk density $\rho = 2300$ kg/m³, gravitational acceleration $g = -9.8$ m/s², contact penalty $P_n = P_s = 100$ GPa. We adopt the unstructured Delaunay triangulation scheme to mesh the model (Fig. 24b), and the rocks are discretized into individual finite elements without cohesion. The model consists of 8,750 triangle elements, and the average element size is 4.2 m. Additionally, we select two monitoring points (i.e., MP-1 and MP-2 in Fig. 24b) to track the evolution of their resultant velocities with time. Note that the friction coefficients between the rocks and between the rock and the sliding base are 0.15 and 0.20, respectively (Wei et al. 2019; Zheng et al. 2014), and the effect of groundwater level on slope sliding is not considered.

The resultant velocities of the two monitoring points with time are presented in Fig. 25a. At the initial stage, rocks slide

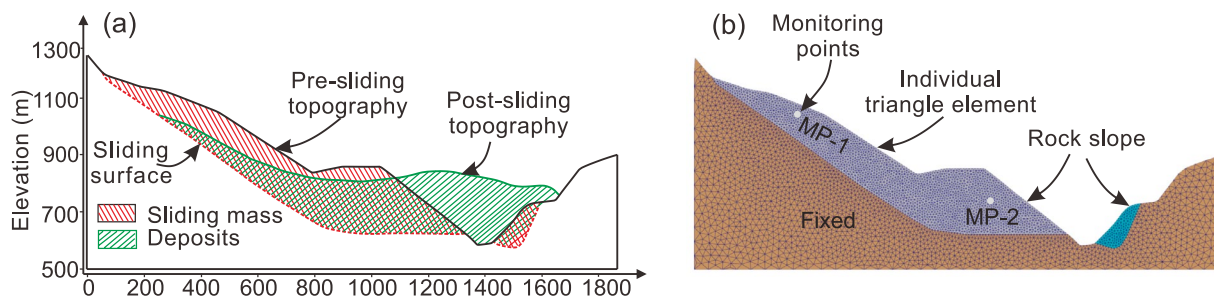


Fig. 24 **a** The typical cross-section of the Vaiont landslide before and after the sliding (modified from Cai et al. 2024). **b** Mesh. Two monitoring points are denoted as MP-1 and MP-2

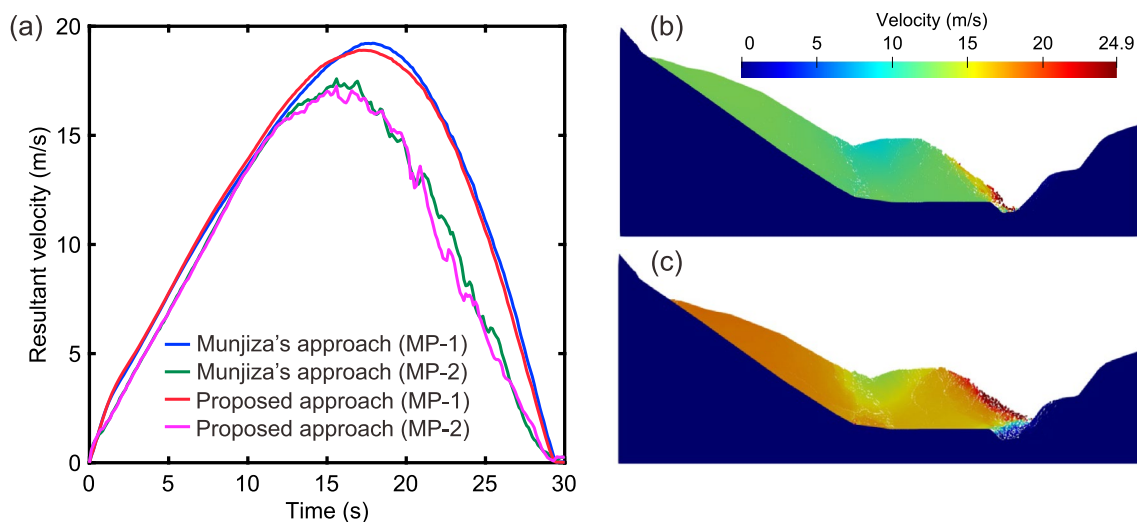


Fig. 25 **a** The resultant velocities at the two monitoring points with time using Munjiza's approach and the proposed approach. Simulation results of the Vaiont landslide at **b** 9 s and **c** 15 s using the proposed approach

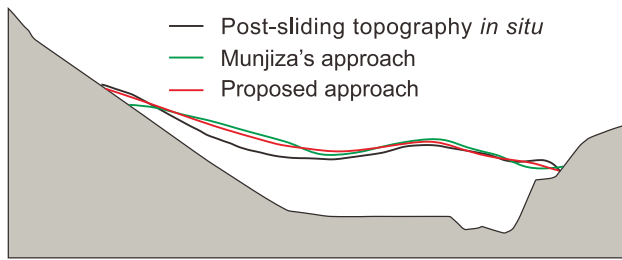


Fig. 26 The comparison of post-sliding topography with the proposed approach, Munjiza's approach and the observations *in situ* at 30 s

down since the resistance force of the rock slope stacked along the sliding surface is insufficient to maintain its stability. The resultant velocities obtained from both Munjiza's approach and the proposed approach increase in a similar trend. The slope also exhibits a similar velocity distribution and moves forward as a whole (Fig. 25b). As the model continues to evolve, the movement of rocks is obstructed by the slope on the other side of the valley (Fig. 25c). Meanwhile, the resultant velocities at the two monitoring points gradually decrease with time. The peak of resultant velocities obtained from Munjiza's approach is slightly larger than that of our proposed approach (Fig. 25a), indicating that the inaccurate evaluation of contact force may yield larger velocities during the violent collision. When the sliding of the rock slope stops, the deposit profiles of the rock slope obtained from the proposed and Munjiza's approaches and the observations *in situ* are presented in Fig. 26. Compared with Munjiza's approach, our proposed approach can better capture the actual topography, which further verifies the accuracy of the proposed approach for rock slope sliding contact simulation.

5 Conclusions

Based on the boundary node lists, a unified distance potential field in 2D FDEM is established to simulate the contact interaction process between discrete bodies with arbitrary shapes. This proposed approach not only overcomes the dependence of contact force on element size but also eliminates the artificial non-smooth transition of contact force. The features of the proposed method to handle complex contact interaction of discrete bodies with arbitrary polygons are summarized as follows. (1) Instead of using the standard potential function, we propose using the boundary node lists to establish a unified distance potential field, in which the nodal potential of nodes associated with boundary elements can be calculated based on the shortest distance between each node and the model boundary. The local distance potential field in the proposed approach can also be updated accordingly when solid fracturing occurs. (2) Within the explicit FDEM framework, formulations

of normal and tangential contact force are systematically given, and the accuracy and robustness of the proposed method for momentum conservation, energy conservation and frictional experiment are also verified. (3) Compared with the existing contact algorithms in FDEM, the proposed approach can deal with complex cases involving relatively large contact areas between contact pairs and arbitrary shape polygons, and it can also overcome the jump of normal contact force direction. For the Brazilian tensile tests, the proposed approach can obtain a more stable mechanical response in terms of the tensile stress curve.

We present two application examples to demonstrate the capability of the proposed approach for predicting the failure patterns of rock slopes. The simulation results reveal that the proposed approach can effectively capture the interaction process of rock blocks, which is expected to provide a new technique to investigate the slumping and sliding failure mechanism of rock slopes. However, we infer that when it comes to 3D simulations involving crack propagation, the computational efficiency will be inevitably reduced due to the time-consuming update of boundary nodes. We are uncertain about the computational cost in 3D at the moment. Nevertheless, we can draw strategies from the recent literature to efficiently update the master–slave lists (Wu et al. 2024), which may help improve the computational efficiency of updating the boundary nodes in 3D. Additional work, including alternative or similar algorithmic solutions in terms of contact models, as well as their extensions to 3D models, will be reported in the near future.

Appendix A: Explicit Solution in FDEM

In 2D FDEM models, the nodal motion equations based on the explicit integration schemes in FDEM can be expressed as (Munjiza 2004)

$$\mathbf{M}\ddot{\mathbf{u}} + \mathbf{C}\dot{\mathbf{u}} = \mathbf{f}, \quad (\text{A.1})$$

where \mathbf{M} is the lumping mass matrix, \mathbf{C} is the damping matrix, \mathbf{u} is the nodal displacement vector, $\dot{\mathbf{u}}$ and $\ddot{\mathbf{u}}$ are the nodal velocity and acceleration vector, respectively, and \mathbf{f} represents the total nodal force vector. The damping matrix is introduced to consume kinetic energy for quasi-static equilibrium cases. The conventional FDEM uses the central difference scheme to update the displacement and velocity of nodes at each simulation time step. Then, the velocity vector $\dot{\mathbf{u}}$ of each node can be obtained by

$$\dot{\mathbf{u}}(t + \Delta t) = \dot{\mathbf{u}}(t) + \ddot{\mathbf{u}}(t) \cdot \Delta t \quad (\text{A.2})$$

where Δt is the time step, and t and $t + \Delta t$ denote the previous and current time instants, respectively. The displacement vector $\mathbf{u}(t + \Delta t)$ of the node can be updated using

$$\mathbf{u}(t + \Delta t) = \mathbf{u}(t) + \dot{\mathbf{u}}(t + \Delta t) \cdot \Delta t \tag{A.3}$$

Unlike the collision of rigid bodies, we can obtain the stress and deformation distribution of bodies during the contact or collision process in FDEM. The mechanical behavior of constant strain finite elements can be expressed by Munjiza (2004)

$$\sigma_{ij} = \frac{\lambda}{2} \left(J - \frac{1}{J} \right) \delta_{ij} + \frac{\xi}{J} (B_{ij} - \delta_{ij}) + \eta D_{ij} \quad (i,j = 1, 2). \tag{A.4}$$

Here

$$B_{ij} = \frac{1}{2} (u_{i,j} + u_{j,i}), \tag{A.5}$$

and

$$D_{ij} = \frac{1}{2} (v_{i,j} + v_{j,i}) \tag{A.6}$$

where σ_{ij} represents the Cauchy stress tensor, λ and ξ are the Lamé constants, $u_{i,j}$ and $u_{j,i}$ are both the deformation gradient tensor, $v_{i,j}$ and $v_{j,i}$ are both the velocity gradient tensor, B_{ij} denotes the left Cauchy-Green deformation tensor, D_{ij} is the rate of deformation tensor, J is the determinant of deformation gradient, η is the viscous damping coefficient, and δ_{ij} is the Kronecker delta.

The boundary conditions are

$$u_i = \bar{u}_i, \quad \sigma_{ij} n_j = T_i, \tag{A.7}$$

and the initial conditions are

$$u_i(x, t = 0) = \bar{u}_i(x), \quad \dot{u}_i(x, t = 0) = \bar{\dot{u}}_i(x), \tag{A.8}$$

where n_j is the outward normal to the external surface, T_i is the component of externally applied traction, u_i is the component of nodal displacement vector \mathbf{u} , and x denotes the global coordinate.

Appendix B: Establishment and Update of Master–Slave Node Lists

As illustrated in Fig. 27a, the whole continuous model domain is discretized into six triangular finite elements, and each node number of finite elements is independent rather than shared. We reserve the mapping information from the original nodes before model discretization (denoted as master nodes, e.g., Nodes j_1 in Fig. 27a) to the corresponding new nodes after model discretization (denoted as slave nodes, e.g., Nodes 0 to 5 in Fig. 27a) in a master–slave manner. We introduce two arrays, $a[]$ and $b[]$, to store the information of master and slave nodes, respectively. Taking the cohesive element C_1 presented in Fig. 27a for example, we have $a[1] = 2, a[10] = 11, b[1] = b[2] = j_1, b[10] = b[11] = j_2$. By looping over all pre-inserted cohesive elements of the solid domain, we can establish the master–slave node lists. For the master node j_1 , we can obtain the mapping list information such as $0 \rightarrow j_1, 1 \rightarrow j_1, \dots, 5 \rightarrow j_1$ and $0 \rightarrow 1 \rightarrow 2 \rightarrow 3 \rightarrow 4 \rightarrow 5 \rightarrow 0$, respectively. Once the solid fracturing occurs (i.e., broken cohesive elements), we need to update the master–slave node mapping list accordingly to accommodate the variance of boundary node lists mentioned in Sect. 2.2.2. As shown in Fig. 27b, if the breakage of cohesive element C_1 and C_2 occurs, we have $a[2] = 3, a[3] = -1, a[4] = 5, a[5] = 0, a[0] = 1, a[1] = -1$ for array $a[]$ and $b[2] = b[3] = j_3, b[4] = b[5] = b[0] = b[1] = j_1$ for array

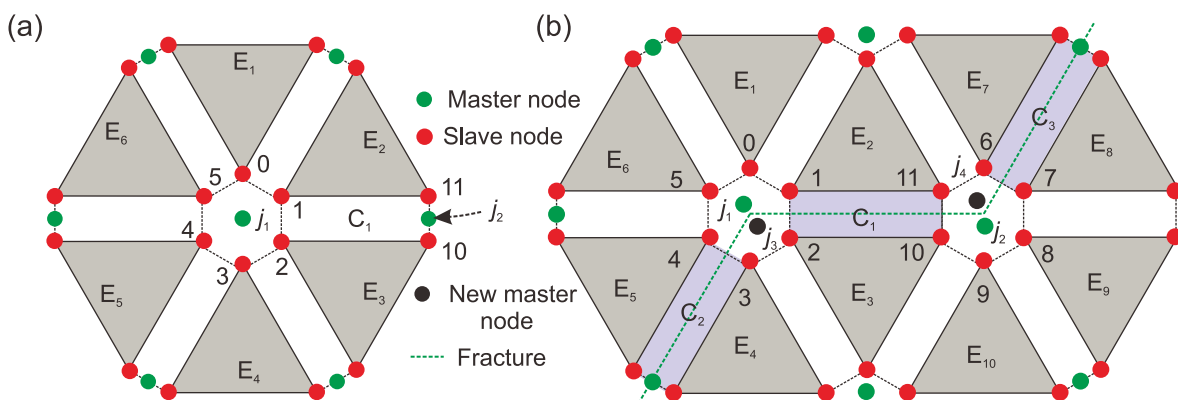


Fig. 27 **a** Establishment and **b** update of master–slave node lists. Nodes j_1, j_2 and j_3, j_4 are old and new master nodes, respectively, and nodes 0 to 11 are slave nodes, where master and slave nodes are denoted by blue and red dots, respectively. The newly generated mas-

ter nodes are marked in black dots. C_1, C_2 and C_3 represent the cohesive elements. The broken cohesive elements (i.e., microcracks) are marked by the light cyan patch

$b[]$. As a result, the slave Nodes 0 to 5 are divided into two groups, and they are respectively mapped to a new master Node j_3 and the old master Node j_1 . The other slave nodes (e.g., 6 to 11) of these invoked cohesive elements should also be processed at the same time in a similar manner.

Appendix C: Fracture Initiation and Propagation in FDEM

To simulate fracture initiation and propagation in rock masses, four-node cohesive elements with zero thickness are initially inserted into the common boundaries between adjacent finite element pairs at the beginning of the simulation (see Fig. 28a, b). The cohesive tractions of each cohesive element, i.e., σ^{coh} and τ^{coh} between the common edges of a triangle finite element pair, is denoted as a function of the relative displacements of the two edges of a cohesive element, i.e., o and $|s|$, in the normal and tangential directions, respectively (see Fig. 28c–e). At present, the fracturing modes of cohesive elements mainly consist of three types, i.e., Mode I (tensile fracturing), Mode II (shear fracturing), and mixed Mode I-II (tensile-shear mixed fracturing). As shown in Fig. 28c, when the normal opening o increases to the elastic limits o_p , the normal cohesive stress

(σ^{coh} , tensile positive) reaches the tensile strength f_t , which marks the damage initiation point of a cohesive element. As o continues to increase, the cohesive element starts to damage. When o reaches the critical (maximum) normal opening o_t , i.e., the breakage point of cohesive element, a pure tensile microcrack will emerge (Mode I). Similarly, as presented in Fig. 28d, the shear cohesive stress (τ^{coh}) reaches the shear strength f_s when the tangential slipping $|s|$ increases to the elastic limits s_p . Specifically, the peak shear strength is defined using the Mohr–Coulomb criterion as

$$f_s = \begin{cases} c & \text{if } \sigma^{\text{coh}} \geq 0 \\ c - \sigma^{\text{coh}} \tan \varphi & \text{if } \sigma^{\text{coh}} < 0 \end{cases}, \quad (\text{C.1})$$

where c and φ are the cohesion and internal friction angle of the cohesive elements, respectively. The cohesive element breakage of the mixed Mode I-II is determined by the combined effect of normal opening and tangential slipping (Fig. 28e). Note that the mixed Mode I-II includes two fracturing scenarios, i.e., tensile-shear fracturing and compressive-shear fracturing. More details on the constitutive laws of cohesive elements can refer to previous works (Fukuda et al. 2019; Han et al. 2020; Tatone and Grasselli 2015).

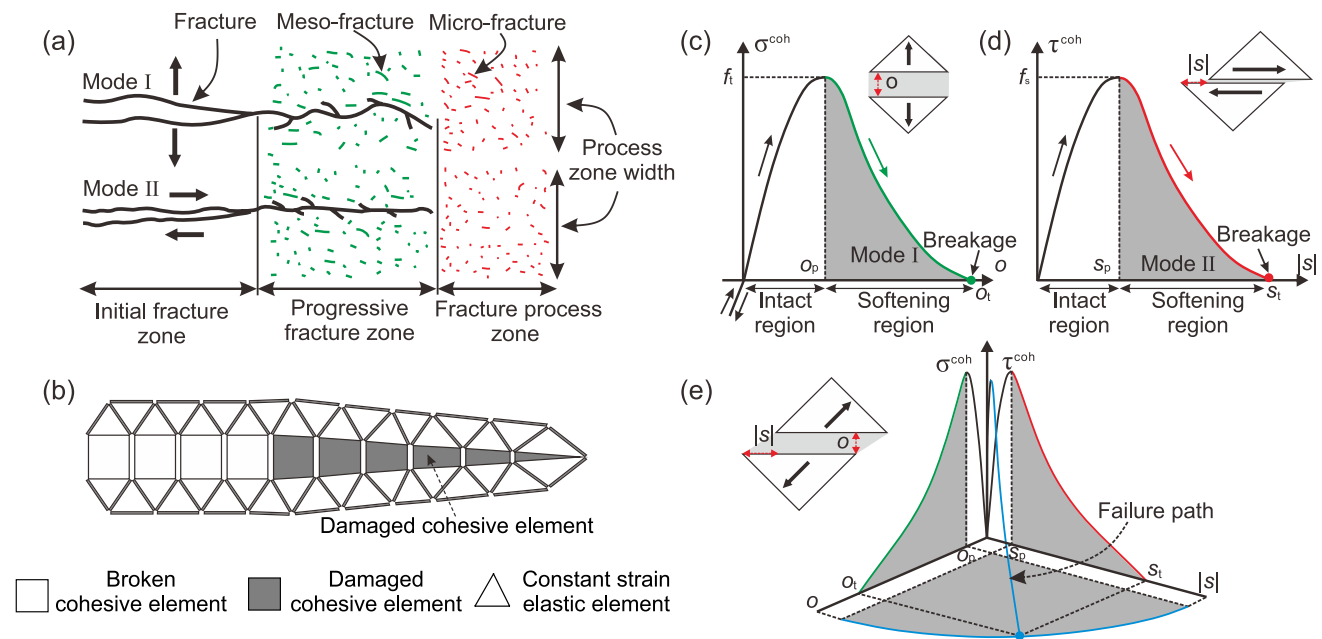


Fig. 28 **a** Conceptual model of FPZ (fracture process zone) development ahead of fracture tip in brittle material (modified from Mohammadnejad et al. 2018). **b** The implementation of FPZ in Mode I in FDEM. **c** Constitutive of tensile fracturing mode, i.e., Mode I. **d** Constitutive of shear fracturing mode, i.e., Mode II. **e** Constitutive of

mixed fracturing mode, i.e., mixed Mode I–II. Here, o and $|s|$ represent the relative opening and slipping displacement of a cohesive element, respectively; o_p and s_p are the elastic limits of o and $|s|$, respectively; o_t and s_t are the critical values of o and $|s|$, respectively; f_t and f_s are the tensile and shear strength of cohesive element, respectively

Author Contributions The authors confirm contributions to the paper as below: Research design: Ke Gao; Analysis of numerical results: Weibing Cai and Shugang Ai; Draft manuscript preparation: Weibing Cai; Revised manuscript and funding support: Ke Gao and Yan Qiao. All authors have reviewed the results and approved the final version of the manuscript.

Funding This work is supported by the Shenzhen Science and Technology Program (JCYJ20220530113612028), the Guangdong Basic and Applied Basic Research Foundation (2023A1515011244), and the Guangdong Provincial Key Laboratory of Geophysical High-resolution Imaging Technology (2022B1212010002).

Data availability The data are available by contacting the corresponding author upon reasonable request.

Declarations

Conflict of interest The authors state that no known conflicts of interest are associated with this publication.

References

- Cai W, Gao K, Ai S, Wang M, Feng YT (2023) Implementation of extrinsic cohesive zone model (ECZM) in 2D finite-discrete element method (FDEM) using node binding scheme. *Comput Geotech* 159:105470
- Cai W, Gao K, Ai S, Zhi S (2024) A 2D energy-conserving contact model for the combined finite-discrete element method (FDEM). *Comput Geotech* 166:105972
- Cundall PA (1988) Formulation of a three-dimensional distinct element model—Part I. A scheme to detect and represent contacts in a system composed of many polyhedral blocks. *Int J Rock Mech Min Sci Geomech Abstr* 25(3):107–116
- Cundall PA, Strack ODL (1979) A discrete numerical model for granular assemblies. *Geotechnique* 29(1):47–65
- Duan K, Li X, Kwok C-Y, Zhang Q, Wang L (2021) Modeling the orientation- and stress-dependent permeability of anisotropic rock with particle-based discrete element method. *Int J Rock Mech Min Sci* 147:104884
- Feng Y (2021a) A generic energy-conserving discrete element modeling strategy for concave particles represented by surface triangular meshes. *Int J Numer Methods Eng* 122(10):2581–2597
- Feng YT (2021b) An energy-conserving contact theory for discrete element modelling of arbitrarily shaped particles: basic framework and general contact model. *Comput Meth Appl Mech Eng* 373:113454
- Feng YT (2021c) An energy-conserving contact theory for discrete element modelling of arbitrarily shaped particles: contact volume based model and computational issues. *Comput Meth Appl Mech Eng* 373:113493
- Feng YT, Owen DRJ (2004) A 2D polygon/polygon contact model: algorithmic aspects. *Eng Comput* 21(2):265–277
- Fukuda D, Mohammadnejad M, Liu H, Zhang Q, Zhao J, Dehkhoda S, Chan A, Kodama J-i, Fujii Y (2019) Development of a 3D hybrid finite-discrete element simulator based on GPGPU-parallelized computation for modelling rock fracturing under quasi-static and dynamic loading conditions. *Rock Mech Rock Eng* 53(3):1079–1112
- Gao W, Feng YT (2019) A coupled 3D discrete elements/isogeometric method for particle/structure interaction problems. *Comput Part Mech* 7(5):869–880
- Han H, Fukuda D, Liu H, Salmi EF, Sellers E, Liu T, Chan A (2020) Combined finite-discrete element modelling of rock fracture and fragmentation induced by contour blasting during tunnelling with high horizontal in-situ stress. *Int J Rock Mech Min Sci* 127:104214
- Hatzor YH, Arzi AA, Zaslavsky Y, Shapira A (2004) Dynamic stability analysis of jointed rock slopes using the DDA method: King Herod's Palace, Masada, Israel. *Int J Rock Mech Min Sci* 41(5):813–832
- Lai Z, Zhao S, Zhao J, Huang L (2022) Signed distance field framework for unified DEM modeling of granular media with arbitrary particle shapes. *Comput Mech* 70(4):763–783
- Latham J-P, Xiang J, Farsi A, Joulin C, Karantouzlis N (2019) A class of particulate problems suited to FDEM requiring accurate simulation of shape effects in packed granular structures. *Comput Part Mech* 7(5):975–986
- Lei Z, Rougier E, Euser B, Munjiza A (2020) A smooth contact algorithm for the combined finite discrete element method. *Comput Part Mech* 7(5):807–821
- Liu Q, Deng P (2019) A numerical investigation of element size and loading/unloading rate for intact rock in laboratory-scale and field-scale based on the combined finite-discrete element method. *Eng Fract Mech* 211:442–462
- Mahabadi OK, Lisjak A, Munjiza A, Grasselli G (2012) Y-Geo: new combined finite-discrete element numerical code for geomechanical applications. *Int J Geomech* 12(6):676–688
- Mathias L, Wouter S, Tom L, Jifí P, Bart S (2021) Packing simulation of thin flexible particles using a novel discrete element model. *Comput Part Mech* 9(3):407–420
- Mohammadnejad M, Liu H, Chan A, Dehkhoda S, Fukuda D (2018) An overview on advances in computational fracture mechanics of rock. *Geosystem Eng* 24(4):206–229
- Munjiza A (2004) *The combined finite-discrete element method*. Wiley, London
- Munjiza A, Andrews KRF (1998) NBS contact detection algorithm for bodies of similar size. *Int J Numer Methods Eng* 43(1):131–149
- Munjiza A, Knight EE, Rougier E (2011) *Computational mechanics of discontinua*. Wiley, London
- Munjiza A (1992) *Discrete elements in transient dynamics of fractured media*. PhD thesis, Swansea University, Swansea, UK
- Nassauer B, Kuna M (2013) Contact forces of polyhedral particles in discrete element method. *Granular Matter* 15(3):349–355
- Potyondy DO, Fu W (2024) A 3D subspring network breakable voronoi model for rock: laboratory-scale behavior. In: *Proceedings of 58th U.S. Rock Mechanics/Geomechanics Symposium*, Colorado, USA, 23–26 June
- Potyondy DO, Cundall PA (2004) A bonded-particle model for rock. *Int J Rock Mech Min Sci* 41(8):1329–1364
- Potyondy DO (2018) A FLAT-JOINTED BONDED-PARTICLE MODEL FOR ROCK. In: *Proceedings of 52nd U.S. Rock Mechanics/Geomechanics Symposium*, Washington, USA, June
- Regassa B, Xu N, Mei G (2018) An equivalent discontinuous modeling method of jointed rock masses for DEM simulation of mining-induced rock movements. *Int J Rock Mech Min Sci* 108:1–14
- Shi GH, Goodman RE (1985) Two dimensional discontinuous deformation analysis. *Int J Numer Anal Methods Geomech* 9(6):541–556
- Sitar N, Maclaughlin M, Tech M (1997) Kinematics and discontinuous deformation analysis of landslide movement. *Panamerican Symposium on Landslides*, Rio de Janeiro, Nov 10–14th
- Tatone BSA, Grasselli G (2015) A calibration procedure for two-dimensional laboratory-scale hybrid finite–discrete element simulations. *Int J Rock Mech Min Sci* 75:56–72
- Wang X, Yin ZY, Xiong H, Su D, Feng YT (2021) A spherical-harmonic-based approach to discrete element modeling of 3D irregular particles. *Int J Numer Methods Eng* 122(20):5626–5655

- Wei W, Zhao Q, Jiang Q, Grasselli G (2019) A new contact formulation for large frictional sliding and its implement in the explicit numerical manifold method. *Rock Mech Rock Eng* 53(1):435–451
- Wu W, Zhu H, Lin J-S, Zhuang X, Ma G (2018) Tunnel stability assessment by 3D DDA-key block analysis. *Tunn Undergr Space Technol* 71:210–214
- Wu D, Fukuda D, Min G, Li H, Liu H, Ogata S, Maeda Y, Zhang Q (2024) Development of a GPGPU-parallelized 3-D FDEM with a novel and simple implementation of extrinsic cohesive zone model. *Comput Geotech* 174:106643
- Yan CZ, Zheng H (2017) A new potential function for the calculation of contact forces in the combined finite-discrete element method. *Int J Numer Anal Methods Geomech* 41(2):265–283
- Zhao L, Liu X, Mao J, Xu D, Munjiza A, Avital E (2018a) A Novel Contact Algorithm Based on a Distance Potential Function for the 3D Discrete-Element Method. *Rock Mech Rock Eng* 51(12):3737–3769
- Zhao L, Liu X, Mao J, Xu D, Munjiza A, Avital E (2018b) A novel discrete element method based on the distance potential for arbitrary 2D convex elements. *Int J Numer Methods Eng* 115(2):238–267
- Zheng W, Zhuang X, Tannant DD, Cai Y, Nunoo S (2014) Unified continuum/discontinuum modeling framework for slope stability assessment. *Eng Geol* 179:90–101
- Zheng F, Jiao Y, Leung YF, Zhu J (2018) Algorithmic robustness for contact analysis of polyhedral blocks in discontinuous deformation analysis framework. *Comput Geotech* 104:288–301
- Zheng F, Zhuang X, Zheng H, Jiao Y-Y, Rabczuk T (2020a) Kinetic analysis of polyhedral block system using an improved potential-based penalty function approach for explicit discontinuous deformation analysis. *Appl Math Model* 82:314–335
- Zheng F, Zhuang X, Zheng H, Jiao Y-Y, Rabczuk T (2020b) A robust potential-based contact force solution approach for discontinuous deformation analysis of irregular convex polygonal block/particle systems. *Acta Geotech* 16(3):679–697
- Zhou X, Chen J (2019) Extended finite element simulation of step-path brittle failure in rock slopes with non-persistent en-echelon joints. *Eng Geol* 250:65–88

Publisher's Note Springer Nature remains neutral with regard to jurisdictional claims in published maps and institutional affiliations.

Springer Nature or its licensor (e.g. a society or other partner) holds exclusive rights to this article under a publishing agreement with the author(s) or other rightsholder(s); author self-archiving of the accepted manuscript version of this article is solely governed by the terms of such publishing agreement and applicable law.